Materials Horizons

This article can be cited before page numbers have been issued, to do this please use: Y. Xiao, Z. Chen, X. Liu, X. Wang, G. Ding, Z. Wang, P. Wang and G. Liao, *Mater. Horiz.*, 2025, DOI: 10.1039/D5MH01487E.

ROYAL SOCIETY OF CHEMISTRY

rsc.li/materials-horizons

View Article Online
DOI: 10.1039/D5MH01487E

Wider impact

Conventional energy production exacerbates global environmental degradation, including climate change and greenhouse effects. Consequently, implementing sustainable renewable energy systems is imperative to mitigate impending energy crises, preserve ecological integrity, and achieve zero-emission targets with solar-driven artificial photosynthesis on advanced semiconductors representing a critical pathway for circular energy cycles. PDI semiconductor photocatalyst prized for its economic viability, operational stability, superior photochemical responds, and electron-accepting capacity. This review systematically chronicles the evolution of PDI-based photocatalytic systems, combined with contemporary synthesis paradigms with emphasis on structural/functional modifications to advance semiconductor photocatalysis for solar energy harvesting. We further delineate persistent research challenges and strategic future directions. The transformative potential of these advanced materials underscores the imperative for cross-disciplinary convergence between materials chemistry and process engineering. Such synergies will catalyze innovative breakthroughs in semiconductor photocatalysis, accelerating the development of sustainable energy technologies. By consolidating design principles, mechanistic insights, and application landscapes, this work provides a foundational framework for researchers engaged in photocatalytic energy conversion and serves as a blueprint for engineering PDI photocatalysts.

View Article Online
DOI: 10.1039/D5MH01487E

Data availability statements

No primary research results, software or code have been included and no new data were generated or analysed as part of this review.

View Article Online
DOI: 10.1039/D5MH01487E

Perylene diimide-based photocatalysts: from molecular design to emerging applications

Yin Xiao[a], Zihe Chen[a], Xin Liu[a], Xusheng Wang[b], Guixiang Ding[a], Zhaoqiang Wang[a], Peng Wang[c,*], and Guangfu Liao[a,*]

[a]College of Materials Engineering, Fujian Agriculture and Forestry University, Fuzhou 350002, China.
[b]State Key Laboratory of Bio-based Fiber Materials, School of Materials Science and Engineering, Zhejiang Sci-Tech University, Hangzhou 310018, China.
[c]CenerTech Tianjin Chemical Research & Design Institute Company, Ltd., Tianjin 300131, China.

*Corresponding authors. E-mail addresses: lzuwangpeng@163.com (P. Wang); liaogf@mail2.sysu.edu.cn (G. Liao)

DOI: 10.1039/D5MH01487E

Abstract

Perylene diimide (PDI)-based semiconductor materials show significant promise for photocatalytic environmental decontamination and the conversion of energy resources but suffer from inefficient photocarriers separation which greatly limits their activity. Consequently, designing PDI-based photocatalysts to enhance carrier separation has become a major research focus. This persistent challenge has positioned the rational design of PDI-based architectures to enhance carrier dissociation kinetics and elevate functional efficacy as a central research thrust in contemporary photocatalysis. This review firstly examines recent progress in the rational design of PDI-based photocatalysts and their charge transfer mechanism. Then, advances in fabrication of PDI photocatalysts and associated electron/hole transfer mechanisms are discussed. It systematically evaluates their enhanced activity in key applications: water splitting, CO_2 reduction, N_2 fixation, and pollutant degradation etc. Subsequently, the fundamental photocatalytic mechanism inherent to PDI-based materials is scrutinized in depth. Finally, outstanding issues and prospective uses for PDI-based photocatalysts are also discussed. It is believed that this review supplies valuable direction for engineering advanced PDI-based photocatalytic systems.

View Article Online
DOI: 10.1039/D5MH01487E

Wider impact

Conventional energy production exacerbates global environmental degradation, including climate change and greenhouse effects. Consequently, implementing sustainable renewable energy systems is imperative to mitigate impending energy crises, preserve ecological integrity, and achieve zero-emission targets with solar-driven artificial photosynthesis on advanced semiconductors representing a critical pathway for circular energy cycles. PDI semiconductor photocatalyst prized for its economic viability, operational stability, superior photochemical responds, and electron-accepting capacity. This review systematically chronicles the evolution of PDI-based photocatalytic systems, combined with contemporary synthesis paradigms with emphasis on structural/functional modifications to advance semiconductor photocatalysis for solar energy harvesting. We further delineate persistent research challenges and strategic future directions. The transformative potential of these advanced materials underscores the imperative for cross-disciplinary convergence between materials chemistry and process engineering. Such synergies will catalyze innovative breakthroughs in semiconductor photocatalysis, accelerating the development of sustainable energy technologies. By consolidating design principles, mechanistic insights, and application landscapes, this work provides a foundational framework for researchers engaged in photocatalytic energy conversion and serves as a blueprint for engineering PDI photocatalysts.

View Article Online
DOI: 10.1039/D5MH01487E

1. Introduction

Global economic and industrial expansion exacerbates two critical challenges: environmental pollution and energy scarcity.[1-8] Semiconductor photocatalysis emerges as a promising technology, efficiently enabling solar-to-chemical energy transformation through photoredox reactions for pollutant degradation,[9-11] CO_2 reduction,[12, 13] and H_2 production [14, 15] This positions it as a key solution for environmental remediation and renewable energy. However, current limitations including short charge carrier lifetimes, insufficient sunlight utilization, poor stability, and low efficiency[16] hinder its practical deployment. Recently, organic semiconductors photocatalysts have proliferated owing to their molecularly adjustable optoelectronic characteristics, structural versatility and cost-effective synthesis, etc, with representative examples including covalent organic frame-works (COFs),[17] metal-organic frameworks (MOFs),[18] organic polymers[19] and organic supra-molecular compounds[20] etc. Supramolecular organic semiconductors now constitute a rapidly developing photocatalytic domain, benefiting from precise synthetic control and broad spectral absorption capabilities. Among the organic semiconductors, PDI has garnered significant scientific attention owing to its synthetic accessibility, cost-efficiency, and sustained functional integrity under photocatalytic conditions. Nevertheless, their photocatalytic performances remain hampered by inefficient charge separation kinetics and limited operational persistence.[21] Dating in 1913, PDI first served as industrial dyes exhibiting robust durability, chemical resistance, thermal stability, lightfastness, and weatherability. The compound further reveals significant electronic properties beyond pigmentation, including substantial luminescence efficiency, excellent photo-stabilization capacity, and strong electron-accepting capability. Nowadays, PDI demonstrates significant applicability across multiple domains including sensors,[22] fluorescent switch,[23] fluorescent probe,[24] photoconductive materials,[25, 26] and organic light-emitting diodes (OLEDs),[27] etc. A landmark 1997 study by Robert et al.[28] identified PDI molecular as a photocatalytic photosensitizer. Through photoinitiated energy transfer mechanisms, it produces singlet oxygen that mineralizes phenolic contaminants (e.g., phenol) within controlled pH regimes.

Relative to molecular PDI, supramolecular constructs demonstrate advanced photocatalytic behavior, reflecting notable recent advancements in organic photocatalyst design.[29-33] Consequently, this has elevated research focus on PDI-based photocatalysts, centering on photogenerated charge behavior, molecular structure-function relationships, and oxidative/reductive reaction mechanisms. Non-covalent interactions-hydrogen bonding, dipole-dipole, π-π stacking, van der Waals, hydrophobic, and electrostatic forces-govern PDI supramolecular assembly. These approaches permit efficient organic photocatalytic architectures through mild, adaptable synthesis, outperforming covalent organic frameworks (COFs) in structural precision and synthetic economy while circumventing elaborate polymerization pathways.

This review analyzes recent progress in PDI-based photocatalytic architectures. Firstly, we introduce the molecular structure of PDI. Secondly, PDI-based photocatalysts are briefly summarized, including modifying the molecular engineering of PDI monomers (such as the substituents of side-chain and bay position), design of PDI polymer, heterojunction engineering (Type-II, Type-Z and Type-S systems), metal deposition/doping, and construction of π-π composite systems, etc. Thirdly, the application of PDI-based photocatalysts including water splitting, CO_2 reduction, N_2 fixation, and pollutant degradation are summarized. Finally, the analysis concludes by outlining persistent challenges and forward-looking strategies for advanced photocatalyst design. This work aims to establish actionable frameworks for developing high-efficiency PDI materials that enable sustainable energy generation and environmental remediation.

2. Molecular structure of PDI

PDI is a derivative of polycyclic aromatic hydrocarbons,[34, 35] featuring a perylene core symmetrically functionalized with dual imide groups (-CONHCO-)[36] Conventionally synthesized via terminal amidation of 3,4,9,10-perylenetetracarboxylic dianhydride (PTCDA) **(Fig. 1a-b)**, its primary modification sites comprise terminal 'imide positions' and peripheral 'bay positions' (carbons 1,6,7,12). Usually, the electron density at the

nodes of the highest occupied molecular orbital (HOMO) and lowest unoccupied molecular orbital (LUMO) of PDI molecules nearly approaches to zero, meaning that side-chain motifs do not readily engage in Π-electron conjugation with a perylene ring and fail to significantly affect the overall electronic structures of PDI molecules. Frontier molecular orbital analysis (**Fig. 1c**) reveals carbon and oxygen dominate HOMO/LUMO composition, while amide nitrogen exhibits negligible orbital contribution.[37] Modifications at the bay position alter the intrinsic energy levels and redox potential of PDI molecules, whereas substitutions at the imide position preserve these fundamental electronic properties and, consequently, their spectral absorption and emission characteristics. This methodology enables strategic modulation of imide substituents to probe structure-photoactivity relationships while conserving intrinsic orbital energetics.

The perylene ring of PDI features a rigid polycyclic π-conjugated framework, driving supramolecular assembly via π-orbital interactions. Typical interplanar distances in these stacked architectures measure 3.4-3.5 Å **(Fig. 1d)**, mirroring graphene's interlayer spacing.[38] Computational studies by Zhu et al. employing density functional theory (DFT) reveal enhanced π-stacking reduces PDI's band gap and lowers both HOMO/LUMO energy levels. Unlike monomers, supramolecular PDI exhibits semiconductor-like continuous bands due to non-covalent molecular ordering.[39] Würthner et al.[40] demonstrated that imide-position substituents modulate stacking configurations through steric and non-covalent effects. PDI aggregates primarily adopt H-aggregate or J-aggregate arrangements. H-aggregates display strong π-orbital overlap and extended conjugation, yielding semiconducting behavior. Conversely, J-aggregates maintain molecular photophysical properties due to reduced

View Article Online
DOI: 10.1039/D5MH01487E

π-coupling. Mechanistic studies show H-aggregates facilitate electron transfer (ET): co-facial stacking creates π-delocalized channels enabling rapid electron migration to oxygen. J-aggregates favor energy transfer (EnT): photoexcitation generates triplet states via intersystem crossing that sensitize **(Fig. 1e)**. Spectroscopically, H-aggregates exhibit hypsochromically shifted absorption with fluorescence quenching and reduced quantum yields[41] while J-aggregates show bathochromic shifts without significant emission loss[42] making them preferred fluorophores.[43] In photocatalysis, H-aggregates demonstrate superior potential due to deeper valence bands, enhanced charge mobility/separation, and stronger oxidative capacity.[44] This performance stems from PDI's planar aromatic structure mediating robust intermolecular π-π interactions.

View Article Online
DOI: 10.1039/D5MH01487E

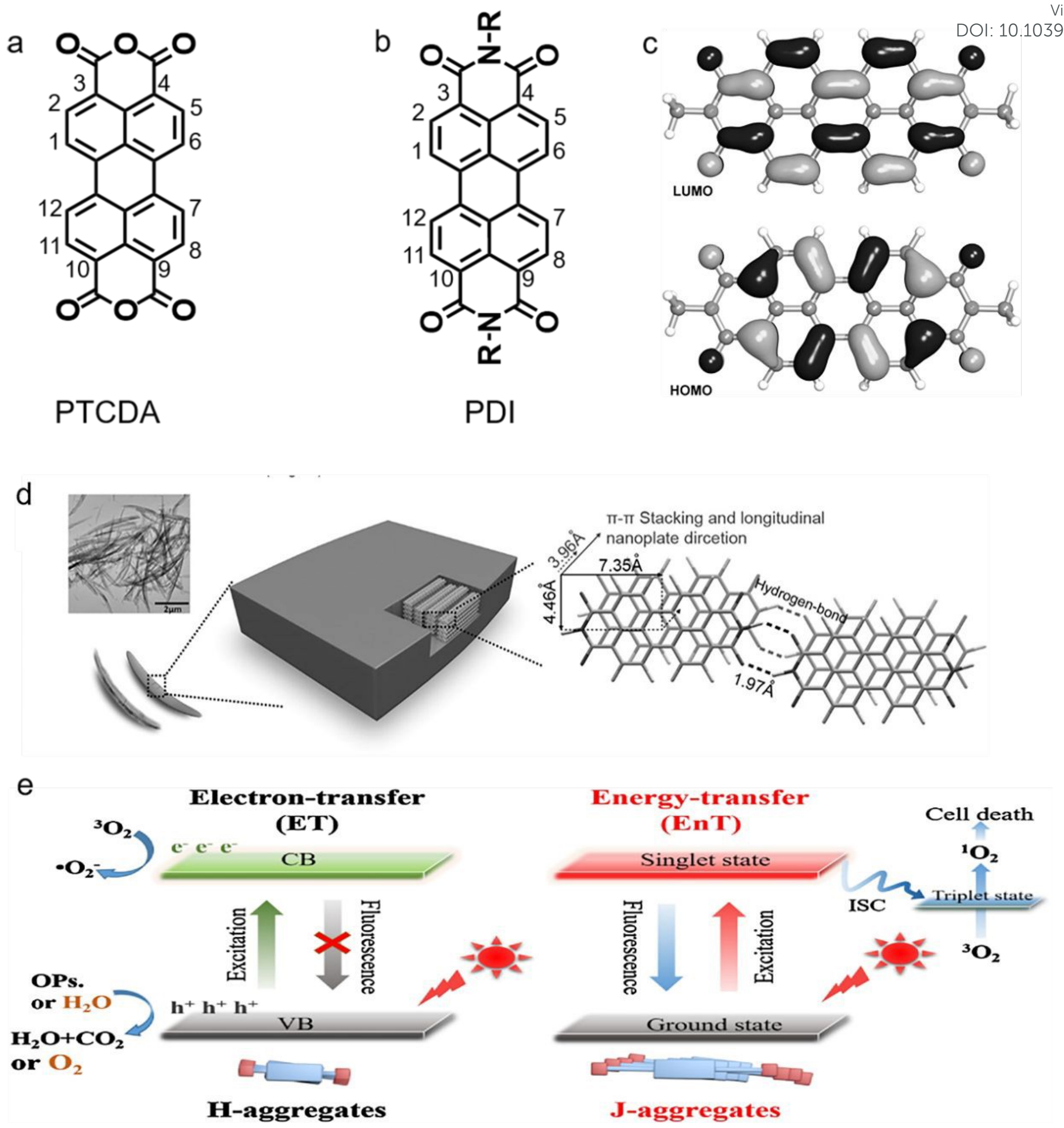

Figure 1 (a) Molecular structures of PTCDA and (b) PDI which show the numbering of the positions in the ring system. (c) DFT calculations of frontier orbitals of N,N'-dimethyl PDI. Reproduced from ref. [37]. Copyright 2011, American Chemical Society. (d) Size of a single PDINH molecule and the π-π stacking distance. Reproduced from ref. [38]. Copyright 2016, Wiley. (e) H/J-aggregated PDI photocatalysts diagram representing the effect of (ET) and (EnT). Reproduced from ref. [41]. Copyright 2018, Elsevier.

3. Modification of PDI-based photocatalysts

Despite emerging as promising photocatalysts, nevertheless, the photocatalytic

View Article Online
DOI: 10.1039/D5MH01487E

performance of PDI supramolecular systems is fundamentally constrained by three principal factors: elevated photogenerated exciton recombination rates, diminished charge transport kinetics, and insufficient oxidative capacity originating from low-lying VB positions.[45] Fundamentally, photocatalytic mechanisms comprise three consecutive processes: (i) photoexcitation across the semiconductor bandgap, (ii) spatial separation and transport of photogenerated charge carriers, and (iii) surface redox reactions. Consequently, rational material modifications primarily target two critical objectives: (i) broadening the spectral response range through bandgap engineering and/or sensitization strategies, and (ii) enhancing charge carrier dynamics by minimizing recombination losses while optimizing mobility pathways.[46] To overcome these inherent constraints, researchers have proposed many methods strategies including design of PDI monomer and polymer, construction of π-π composite systems and heterojunctions system et al. This section provides a critical evaluation of contemporary advancements in enhancing the photocatalytic performance of PDI-based photocatalysts via these methods.

3.1 Monomer modification engineering

PDI, an n-type organic semiconductor and high-grade dye, features a polycyclic aromatic structure with electron-rich perylene core and electron-withdrawing imide groups. This conjugation enables efficient charge carrier migration. PDI monomer architecture-determined by planar conjugation extent, substituent properties, and dipole moment-modulates intermolecular interactions (π-π stacking, electrostatic forces, hydrophobic effects, steric constraints). These interactions govern electronic wavefunction overlap and interchromophoric coupling, enabling precise engineering of supramolecular band structures. In this section, we primarily discuss the influence of substituent groups on the molecular properties of PDI monomers (**Table 1** and **Figure 3**). Substitution at the imide (N-substitution) and bay positions of PDI molecules serves as a fundamental strategy for precisely tuning their photophysical properties, molecular stacking behavior, and photocatalytic performance.

View Article Online
DOI: 10.1039/D5MH01487E

3.1.1 Side-chain substituents

The imide side-chain substituents of PDI molecular serve as critical structural determinants that govern solubility characteristics, supramolecular organization, and consequently, photocatalytic performance metrics. Through deliberate side-chain functionalization, precise modulation of intermolecular packing geometries, charge carrier dynamics, and optoelectronic properties can be achieved. Synthetically, PDIs are typically prepared via condensation of 3,4,9,10-perylenetetracarboxylic dianhydride (PTCDA) with functional groups (alkyl, amino, carboxyl, or aromatic moieties), under an inert atmosphere, employing solvents such as tetrahydrofuran, imidazole, or quinoline, etc., as the solvent, which primarily regulates intermolecular interactions and solubility. This section presents a comprehensive analysis of side-chain classification, systematically evaluating their respective merits and limitations, while elucidating their profound influence on fundamental photocatalytic parameters including electronic band structure, charge transport efficiency, and interfacial charge transfer kinetics.

Alkyl chains, as one of the most prevalent imide side-chain modifications in PDI systems, demonstrate substantial influence on photocatalytic performance through three primary mechanisms: solubility modulation, molecular packing control, and charge transfer regulation. From a solubility perspective, the introduction of alkyl chains effectively attenuates the strong intermolecular π-π interactions characteristic of PDI derivatives. This attenuation effect not only prevents excessive molecular aggregation but also significantly enhances solubility in organic solvents including chloroform and toluene.[47-50] The resultant increase in accessible catalytically active sites substantially improves interfacial contact between the photocatalyst and organic substrates. However, the inherent nonpolar nature of alkyl chains presents limitations in polar reaction media.[51] Specifically, their weak interactions with aqueous phases and metal oxide surfaces create substantial barriers for efficient charge transfer processes in aqueous photocatalytic systems, as evidenced by reduced quantum yields in water-splitting applications. Regarding molecular organization, alkyl chains -

particularly those with optimized length (C6-C12) and branching patterns - induce a distinctive J-type stacking configuration through steric repulsion effects. This packing mode exhibits two critical characteristics: (1) it generates a moderately widened bandgap (2.2-2.5 eV) due to decreased orbital overlap, and (2) facilitates the formation of highly ordered one-dimensional nanostructures.[52] Spectroscopically, the J-aggregation induced by alkyl side chains produces a pronounced bathochromic shift in the absorption spectrum. This redshift effect extends the visible light harvesting range to longer wavelengths (λ >550 nm),[53] thereby enhancing solar energy utilization efficiency in optimized systems. While the application of alkyl-modified PDIs in polar reaction environments remains challenging, their unparalleled ability to precisely control fundamental material properties makes them indispensable for photocatalytic applications involving nonpolar substrates. The structure-property relationships established in these systems provide valuable design principles for developing advanced organic photocatalysts. For instance, Wang et al.[41] synthesized PDI derivatives with different alkyl chain lengths (H-PDI and J-PDI) via a pH-triggered hydrogelation method, systematically investigating the influence of side-chain substituents on photocatalytic performance. The study revealed that H-PDI with shorter side chains formed face-to-face π-π stacking, known as H-aggregation, exhibiting semiconductor characteristics with a narrowed bandgap of 1.69 eV. This configuration predominantly facilitated electron transfer, generating superoxide radicals and holes, which demonstrated superior activity for phenol degradation under visible light with a rate constant of 0.195 h^{-1}. In contrast, J-PDI with longer side chains adopted a head-to-tail stacking mode, referred to as J-aggregation with a bandgap of 1.78 eV, which promoted energy transfer and efficiently produced singlet oxygen with a high quantum yield of 0.66. Under 600 nm red light irradiation, J-PDI exhibited significantly enhanced inhibition of HeLa cells compared to H-PDI. This work elucidates how side-chain engineering can precisely modulate supramolecular packing to optimize photocatalytic pathways, providing a novel strategy for designing tailored photocatalysts for environmental remediation and antitumor applications.

Aromatic or rigid side chains, such as phenyl, naphthyl, or cycloalkyl groups (e.g., 4-tert-butylphenyl), exert a distinct influence on the photocatalytic performance of PDI molecules through their impact on molecular stacking, stability, and electronic interactions.[52] These rigid aromatic moieties strengthen intermolecular π-π stacking via additional aromatic interactions, which enhances charge delocalization across the PDI backbone and improves photostability by reducing structural fluctuations under light irradiation-an advantage for long-term catalytic reactions. However, their large steric volume and strong intermolecular interactions lead to poor solubility in both organic solvents and aqueous media, limiting the processability of PDI and potentially causing excessive aggregation that reduces the accessible catalytic active sites.[54] In terms of molecular packing, aromatic side chains induce a face-to-face H-type stacking mode with a relatively small d-spacing (approximately 3.5 Å), which narrows the band gap of PDI, enabling stronger absorption of visible light. Nevertheless, the tight and rigid stacking increases carrier scattering, resulting in lower charge mobility compared to alkyl-modified PDI. This trade-off between strong light absorption and moderate charge mobility makes aromatic-modified PDI particularly suitable for photocatalytic reactions requiring high oxidizing power and selectivity. Overall, aromatic or rigid side chains play a unique role in optimizing PDI's performance in selective organic synthesis and reactions demanding high stability.[55] For example, Zhu et al.[56] implemented a σ-spacer length optimization strategy to augment charge mobility in imidazole-alkyl-perylene diimide (IMZ-alkyl-PDI) photocatalysts with donor-spacer-acceptor (D-σ-A) architecture through precise π-π stacking distance regulation **(Figure 2a)**. Among the series-non-alkylated (C0IPDI), ethyl-bridged (C2IPDI), and propyl-modified (C3IPDI)-the ethyl linkage achieved minimal π-π separation (3.19 Å) by steric minimization between donor/acceptor units, elucidating intrinsic photocarrier transport mechanisms. C2IPDI demonstrated exceptional photocatalytic enhancement: 32-fold greater phenol degradation efficiency versus IMZ-PDI, alongside a 271-fold increase in oxygen evolution. **(Figure 2b-c)**. Moreover, Sun and coworkers[33]

View Article Online
DOI: 10.1039/D5MH01487E

engineered an ultrathin porous hp-PDI-NA photocatalyst via nicotinic acid terminal substitution **(Figure 2d)**. It demonstrated 3.5-fold higher visible-light phenol degradation activity than nano-PDI, achieving near-complete mineralization. The catalyst retained 98% activity after 5 cycles, and effectively mineralized antibiotics (oxytetracycline) and hormones (ethinylestradiol) **(Figure 2e)**. Combined characterization/theory revealed its enhanced performance stems from a bi-planar conformation and hierarchically porous nanosheet morphology. NA substitution reduces steric hindrance, strengthens π-π conjugation, and shortens interlayer spacing, thereby boosting carrier separation/transport and structural stability **(Figure 2f)**. Although aromatic substituents further extend conjugation, narrowing the bandgap for enhanced visible-light absorption which offers critical advantages including improved processability for homogeneous composite formation, tunable stacking distances for efficient charge transport, and increased surface hydrophilicity to facilitate pollutant adsorption and water activation, bulky groups may disrupt π-conjugation and increase charge transport resistance, excessive intermolecular interactions can reduce active site accessibility, and chemically unstable substituents (e.g., certain alkyl amines) may degrade under prolonged irradiation, compromising catalytic durability. To enhance photocatalytic performance, functional group modifications are employed.

Polar functionalized chains, such as those bearing carboxyl (-COOH)[39, 57]or amine (-NH_2)[58] groups (e.g., glycine or polyethylene glycol derivatives), play a crucial role in regulating the photocatalytic performance of PDI molecules through their influence on solubility, intermolecular interactions, and heterojunction formation. These polar groups significantly enhance the water solubility of PDI, addressing the issue of poor dispersibility in aqueous systems that limits the accessibility of catalytic active sites, thereby facilitating contact with water-soluble pollutants and improving reaction kinetics. Additionally, the polar nature of these side chains enables strong hydrogen bonding or electrostatic interactions with metal oxides (e.g., TiO_2, BiOCl, etc) or metal ions (e.g., Zn^{2+}),[59] which is critical for the formation of stable heterojunctions; such heterojunctions promote efficient interfacial charge

View Article Online
DOI: 10.1039/D5MH01487E

transfer, reducing the recombination rate of photogenerated electrons and holes. For instance, carboxyl-functionalized PDI can form a close heterojunction with BiOCl,[60] where the interfacial charge transfer is accelerated, significantly increase in the generation of hydroxyl radicals (·OH) and a threefold enhancement in phenol degradation efficiency compared to alkyl-modified PDI. However, these polar side chains can also induce excessive intermolecular interactions, leading to H-type aggregation in some cases, which may narrow the visible-light absorption range and increase electron-hole recombination, thereby partially offsetting the positive effects. In terms of molecular stacking, the polar interactions between these side chains tighten the π-π stacking, which narrows the band gap of PDI, allowing for better utilization of visible light. Overall, polar functionalized chains are particularly advantageous in aqueous photocatalytic systems and heterojunction-based catalytic systems, despite their potential to induce unfavorable aggregation, their ability to enhance solubility and promote charge transfer makes them indispensable in optimizing PDI's photocatalytic performance. For example, Li et al.[30] engineered an intralayer polarization field within amide-functionalized PDI supramolecular assemblies (sAmi-PDI) **(Figure 2g)**. π-π stacking and hydrogen bonding synergistically enhance polarization while constructing electron-hole transfer bridges and accelerating carrier separation. The acidic medium optimized electrostatic interactions and provided abundant electron donors/acceptors, boosting self-assembly efficiency. Benefitting from these effects, sAmi-PDI exhibited twofold-enhanced photocatalytic activity in pollutant degradation. The polarization field-originating from supramolecular networks-enables rapid carrier migration, establishing a green synthesis paradigm for high-performance PDI photocatalysts **(Figure 2h-i)**. Guo et al.[61] synthesized engineered an oxygen-deficient PDI supramolecular system (R-Ov-PDI) to optimize hole migration kinetics. Photoinduced holes were preferentially trapped at anionic defect centers, triggering an attack on the C-N bond. Remarkably, visible-light-driven benzylamine photooxidation achieved a benchmark efficiency of 31.3 mmol·g^{-1} h^{-1} with >99% imine selectivity. Moreover, Kong et al.[62]

engineered the preparation of a non-covalent self-assembled phosphoric acid-substituted PDI (PMPDI) **(Figure 2j)**. Functionalization with electron-withdrawing terminal groups **(Figure 2k)** enhanced photocatalytic performance through improved exciton dissociation and extended photon harvesting range. Pu et al.[57] synthesized a series of asymmetrically structured PDI supramolecular photocatalysts (PDI-CH_3, PDI-NH_2, and PDI-COOH) via terminal group modification of imide positions, aiming to enhance the internal electric field (IEF) through molecular dipole engineering. Density functional theory (DFT) calculations revealed that the electron-withdrawing -COOH group in PDI-COOH induced the largest dipole moment (2.3257 D), followed by PDI-NH_2 (1.1715 D) and PDI-CH_3 (0.0034 D), directly correlating with IEF intensity (PDI-COOH: 8.4× PDI-CH_3). This enhanced IEF significantly improved charge separation efficiency from 4.6% (PDI-CH_3) to 11.2% (PDI-COOH), as confirmed by photoelectrochemical tests and surface photovoltage spectroscopy. The work demonstrates that asymmetric molecular design amplifies IEF to simultaneously boost oxidative and reductive photocatalytic activities, offering a universal strategy for organic photocatalyst optimization.

View Article Online
DOI: 10.1039/D5MH01487E

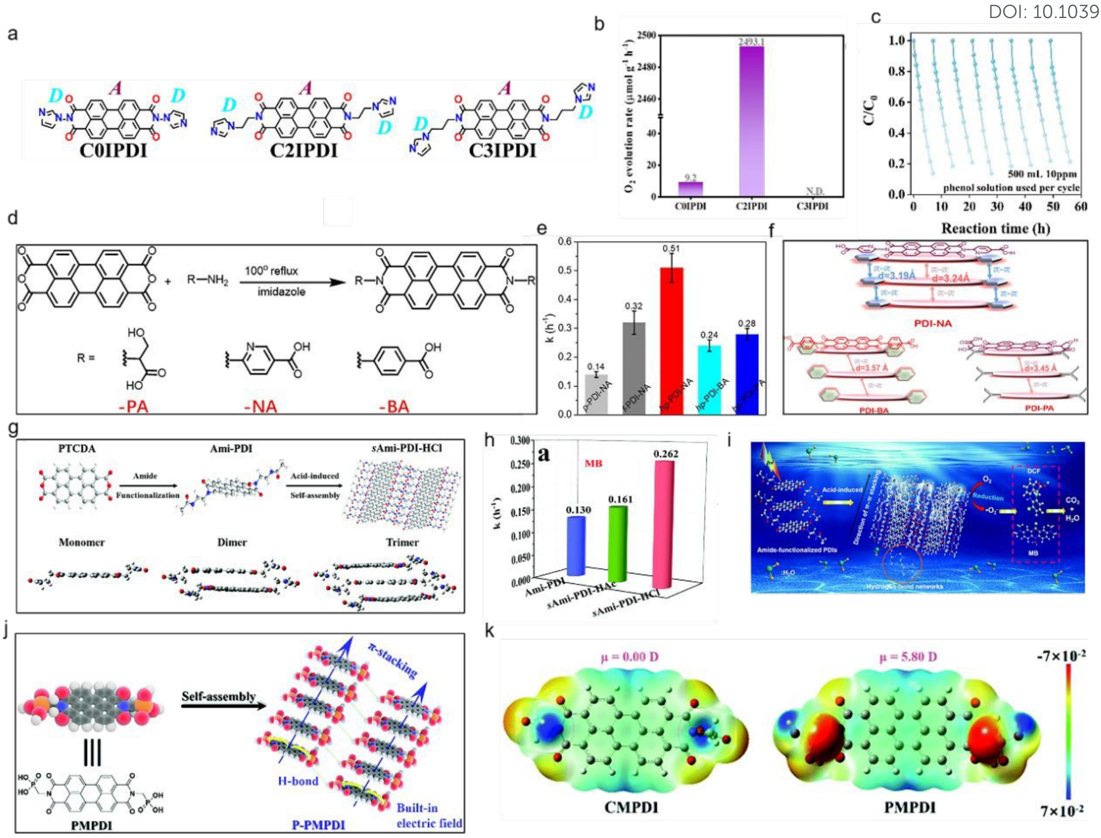

Figure 2. (a) Different σ lengths of molecular structures about CnIPDI. (b) Comparison of photocatalytic O_2 evolution rate on CnIPDI. (c) Cyclic stability of C2IPDI. Reproduced from ref. [56]. Copyright 2023, Wiley. (d) Methods of PDI-NA molecular and reference catalyst. (e) TOC removal rate and mineralization rate constant over different photocatalysts. (f) The schematic diagram of PDI-NA, PDI-BA and PDI-PA. Reproduced from ref. [33]. Copyright 2022, Elsevier. (g) The synthesis process and structure of *s*Ami-PDI-HCl (over) and the DFT calculations about geometries of *s*Ami-PDI-HCl monomers, dimers, and trimers (below). (h) The kinetics constants toward MB. (i) The mechanism for the photocatalytic degradation process when using amide-functionalized supramolecular PDI. Reproduced from ref. [30]. Copyright 2020, the Royal Society of Chemistry. (j) The synthesis of supramolecular P-PMPDI. (k) Diagram of molecular dipoles and electron distribution in PDI derivatives. Reproduced from ref. [62]. Copyright 2019, the Royal Society of Chemistry.

View Article Online
DOI: 10.1039/D5MH01487E

3.1.2 Bay sites substituents engineering

Functionalization of the bay sites in PDI molecules through electron-withdrawing or electron-donating groups represents a viable strategy for modulating both the electronic properties of individual PDI units and their subsequent supramolecular organization. As discussed in the referenced studies,[63] bay sites substituents are critical for tailoring photocatalytic performance through their modulation of molecular geometry, stacking modes (modification to perylene rings would affect PDI self-assembled arrangements since perylene rings are twisted more seriously originated from steric hindrance of substituents), and electronic properties, with distinct advantages and limitations associated with specific substituent types.[64, 65] Halogens (e.g., Cl)[66] and electron-withdrawing groups[67] are prominent examples: halogenation enhances intermolecular π-π stacking by reducing steric hindrance, leading to ordered one-dimensional packing with a d-spacing of ~3.3-3.5 Å, which facilitates efficient charge delocalization and increases electron mobility, while cyano groups lower the LUMO energy level, promoting electron transfer to O_2 for the generation of reactive oxygen species (e.g., $\cdot O_2^-$) crucial for pollutant degradation;[67] However, excessive substitution can induce torsional angles in the perylene core, disrupting the planar π-conjugation and widening the band gap, thereby reducing visible-light absorption efficiency, and bulky substituents (e.g., phenoxy groups) may weaken π-π interactions, resulting in loose stacking and increased carrier recombination.[65] These substituents directly govern stacking modes, which in turn dictate photocatalytic activity. For example, Zhang et al.[66] synthesized three PDI molecules with different bay substitutions: H_2PDI, $2Br\text{-}H_2PDI$, and $4CH_3CH_2O\text{-}H_2PDI$ which formed 1D nanorods, 2D nanosheets, and 0D nanoparticles respectively. The bay substitutions altered the molecular geometry and stacking modes: H_2PDI had a planar structure with strong π-π stacking, $2Br\text{-}H_2PDI$ showed a twisted perylene core with weakened π-π interactions but enhanced hydrogen bonding; $4CH_3CH_2O\text{-}H_2PDI$ exhibited significant distortion due to steric hindrance, leading to loose stacking. These structural changes directly affected the photocatalytic performance: had narrower band gaps (1.62 eV and 1.68 eV vs. 2.02 eV of H_2PDI), 2Br-H_2PDI, and 4CH_3CH_2O-H_2PDI improved charge separation and transfer efficiency, as evidenced by higher photocurrent density and lower electrochemical impedance. Consequently, they displayed superior photocatalytic activity, 2Br-H_2PDI with achieving 11-fold and 1.4-fold higher rates in oxygen evolution reaction (OER) and generation H_2O_2 than H_2PDI, while 4CH_3CH_2O-H_2PDI showed 20-fold and 4-fold enhancements, respectively. Notably could efficiently produce H_2O_2 from O_2 and H_2O without sacrificial agents, demonstrating the critical role of bay substitution in regulating PDI's photocatalytic performance through structural modulation.

View Article Online
DOI: 10.1039/D5MH01487E

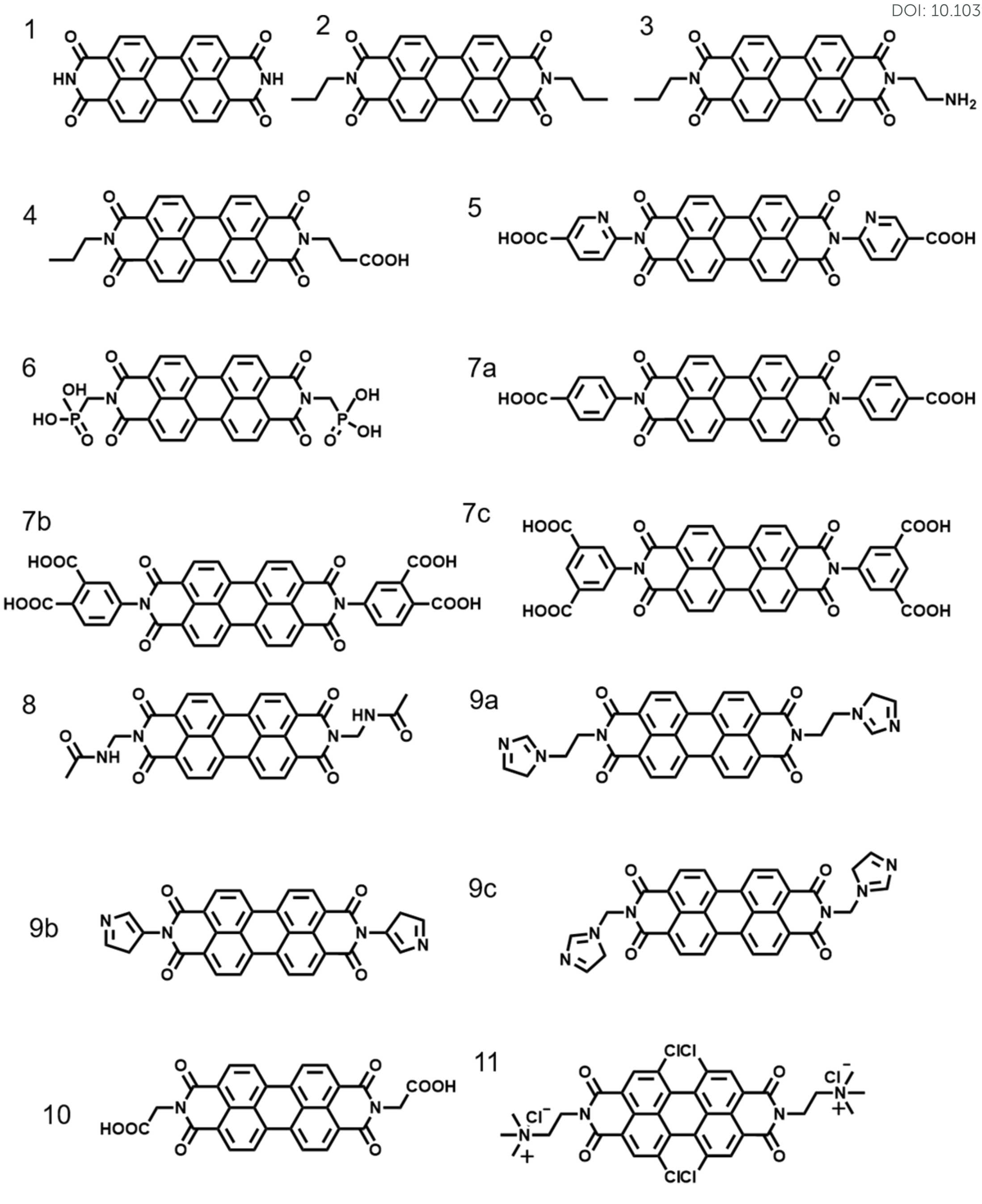

Figure 3. Structures of PDI photocatalysts modified by imide-positions and bay-positions.

Table 1. Summary of the photocatalytic activity of PDI monomers photocatalysts

Photocatalysts	The amount of catalysts	Morphology	Source of light	Photocatalytic application	Performance	AQY	Ref
1	25mg	nanosheets	Xenon lamp, 300W, λ>420nm	Pollutant Phenol	1.23 (h^{-1})	/	68

View Article Online
DOI: 10.1039/D5MH01487E

				Catechol	1.46 (h^{-1})		
				BPA	2.77 (h^{-1})		
				4-CP	2.08 (h^{-1})		
4	25mg	nanobelts	White LED, 5W	Pollutant		/	57
				TC	0.71 (h^{-1})		
				MB	1.24 (h^{-1})		
				RhB	0.55 (h^{-1})		
5	25mg	ultrathin nanosheets	Xenon lamp, 500W, λ>420nm	Pollutant			33
				Phenol	0.51 (h^{-1})		
				OTC	0.65 (h^{-1})		
				EE	0.55 (h^{-1})		
6	50mg	nanobelts	Xenon lamp, 300W, λ>420nm	H_2 production	11700 (μmol $h^{-1}g^{-1}$)	2.96 (550nm)	62
7	25mg	nanosheets	Xenon lamp, 300/500 W, λ>420nm,	Pollutant Phenol/ O_2 production	1.45 (h^{-1}) 2490 (μmol $h^{-1}g^{-1}$)	/ /	69
8	25mg	2D layers with flaky	Xenon lamp, 1000W, λ>420nm	Pollutant		/	30
				MB	0.262 (h^{-1})		
				DCF	0.172 (h^{-1})		
9	25mg	nanobelt	Xenon lamp, 500W, λ>420nm	Pollutant Phenol /O_2 production	3.96 (h^{-1})/ 11700 (μmol $h^{-1}g^{-1}$)	/	56
10	25mg	nanofibers	Xenon lamp,500W, λ>420nm	Pollutant Phenol	0.129 (h^{-1})	/	39
11	/	/	white LED array	H_2O_2 production	/	<1%	70

View Article Online
DOI: 10.1039/D5MH01487E

3.2 Polymer modification engineering

The limited stability of PDI supramolecular materials, stemming from weak non-covalent interactions, presents a significant challenge. Replacing these interactions with directional covalent linkages between PDI monomers would simultaneously enhance structural integrity and preserve the uninterrupted π-delocalization channels essential for rapid electron migration. Zhang's group[71]fabricated crystalline Urea-PDI materials, achieving an oxygen evolution rate of 3223.9 μmol μmol g^{-1} h^{-1} with an apparent quantum yield (AQY) of 3.86% at 450 nm illumination. **(Figure 4a-b)**. The combined effect of crystallinity and molecular dipole moment established a potent IEF. This configuration facilitated effective charge separation and sustains photocatalytic activity for over 100 hours. **(Figure 4c)**. Subsequently, Cao's work[72] 1D Co-UPDI nanocrystals via Co^{2+}-UPDI assembly, achieving a record POE rate in $AgNO_3$ colloids, which was 10 times higher than UPDI. Co-N coordination enhances H-stacking rigidity and enabled in-situ CoOOH formation. Wu et al.[73] prepared non-continuous conjugated semiconductor EDA-PTCDA nanosheets using an uncomplicated solvothermal approach assisted by acidification **(Figure 4d)**. Significant molecular dipole anisotropy enabled efficient partitioning and trapping of photogenerated electron-hole pairs. This polymer demonstrates stable, continuous reactive oxygen species (ROS) production under natural sunlight, conferring effective microbicidal action against both Gram-positive and Gram-negative bacterial strains (**Figure 4e)**. Huang's[74] group synthesized a 3D porous PDI-CTS polymer photocatalyst with a donor-acceptor (D-A) structure. It exhibited a remarkable bisphenol A degradation rate (0.343 min^{-1}) through persulfate radical generation. Donor-acceptor synergy accelerated interfacial charge migration, creating a larger dipole moment and a 6.9-fold stronger IEF than pure PDCTA, greatly facilitating photogenerated carrier separation. Recently, Huang et al.[75] synthesized m-, p-, and o-PDI polymers by coupling PDI with benzene diamines at distinct positions to enhance charge carrier separation **(Figure 4f)**. Distinct linkage configurations modulated specific surface area, band energetics, and charge transport

View Article Online
DOI: 10.1039/D5MH01487E

behavior. Among these, m-PDI demonstrated maximal interfacial exposure and the most negative VB position, while its distinctive architecture enhanced ofloxacin (OFL) adsorption affinity and electron transfer kinetics. Consequently, m-PDI achieved a 0.07481 min^{-1} OFL degradation rate (60 min, light) with robust stability in aquatic environments **(Figure 4g-h)**. Recent representative studies highlight three principal merits of (PDI)-based polymers: (1) Inherent high crystallinity substantially improves charge transport efficiency; (2) Significant molecular dipoles facilitate formation of intensified IEF, enabling accelerated movement of photoinduced charges; (3) Relative to supramolecular PDI systems, covalently bonded architectures demonstrate enhanced structural. integrity.

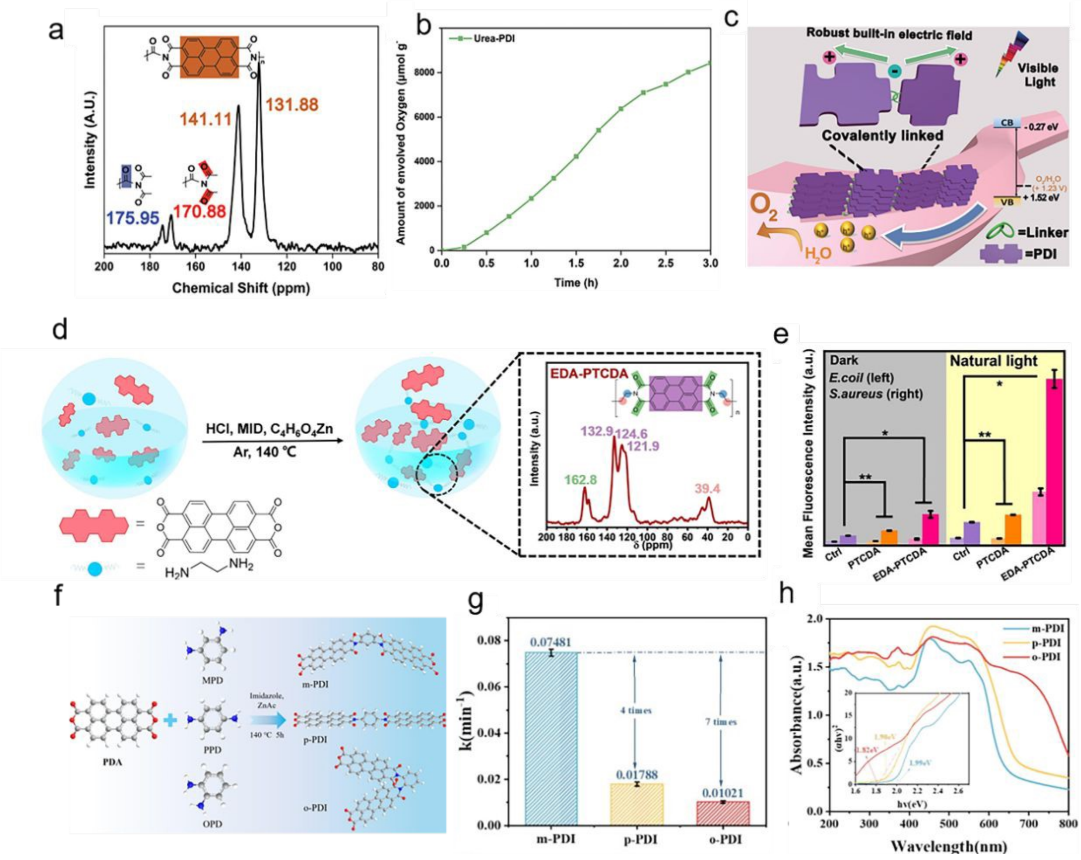

Figure 4. (a) Solid^{13}CNMR spectrum of Urea-PDI. (b) The photocatalytic oxygen evolution with Urea-PDI. (c) Mechanism diagram of the Urea-PDI polymer photocatalyst. Reproduced from ref. [71]. Copyright 2020, Wiley. (d) EDA-PTCDA synthetic methods and solid state^{13}C NMR spectrum. (e) Quantitative analysis of intracellular ROS before and after natural light irradiation. Reproduced from ref. [73].

View Article Online
DOI: 10.1039/D5MH01487E

Copyright 2023, Wiley. (f) Diagram of photocatalyst synthesis. (g) Comparison of degradation rate constants of three materials. (h) UV-vis absorption spectra of m-PDI, p-PDI and o-PDI. Reproduced from ref. [75]. Copyright 2024, Elsevier.

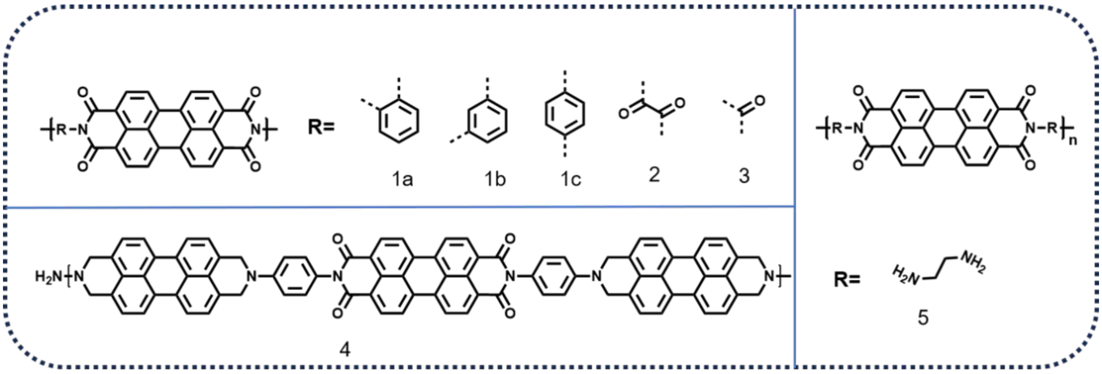

Figure 5. Structure of PDI polymer photocatalysts.

Table 2. Summary of the photocatalytic activity of PDI polymer typical photocatalysts

Photocatalysts	The amount of catalysts	Morphology	Source of light	Photocatalytic application	Performance	AQY	Ref
1a	/	uniform nanosheet	AM1.5G	Watter splitting	Photocurrent density 115.1 (μA cm^{-2})	/	[76]
2	25mg	Ultrathin sheets	Xenon lamp, 300W	O_2,	5110.25 (μmol h^{-1}g^{-1})	2.15 (420nm)	[77]
3	25mg	nanobelt	Xenon lamp, 300W, λ>420nm	O_2,	3223.9 (μmol h^{-1}g^{-1})	3.86 (450nm)	[71]
4	10mg	layer structure	LED lamp, 100W	Pollutant Cr	2.04 (h^{-1})	/	[78]
5		nanosheets	Natural light source	Antibacterial Escherichia coli/Staphylococcus	within 60/45 min	/	[73]

aureus

3.3 Heterojunction engineering

While a narrow bandgap enhances solar energy utilization in photocatalysts, it concomitantly promotes photoinduced charge recombination. Conversely, wide bandgaps suppress recombination and preserve strong redox potentials for charge carriers, yet excessively wide gaps limit broad-spectrum photon harvesting. To resolve this trade-off-termed the ‘single-component bottleneck’-heterojunction engineering provides an effective strategy. Heterojunction photocatalysts comprise two or more distinct semiconductor components, establishing an IEF at their material interfaces. This IEF serves as the primary impetus for photogenerated charge transfer, effectively prolonging carrier lifetimes while minimizing recombination rates.[79-81] This approach increases the lifetime of photo-generated charges and reduces their recombination. In addition, the construction of a heterojunction can also optimize the band positions and facilitate surface catalytic reactions. Contemporary advances in PDI-based heterojunctions utilize these principles to boost photocatalytic efficiency for solar fuel production and pollutant degradation. These systems are categorized primarily by charge transfer mechanism into three classes: type-II, Z-scheme, and S-scheme heterojunctions incorporating PDI. The subsequent portion methodically reviews seminal recent developments in PDI-based heterostructure photocatalysts.

3.3.1 PDI-based type-II heterojunction

In Type-II heterojunction photocatalysts, as shown in **(Figure 6**, type-II heterojunctions possess a staggered gap. Semiconductor A exhibits higher conduction band (CB) and valence band (VB) energies relative to those of semiconductor B. Following photon absorption, thermodynamic gradients propel electrons toward semiconductor B’s CB and holes toward semiconductor A’s VB. This charge

View Article Online
DOI: 10.1039/D5MH01487E

redistribution establishes an IEF, which further promotes directional segregation of charge carriers. Therefore, electrons accumulate in Semiconductor B while holes localize in Semiconductor A, significantly enhancing photocatalytic activity. Significantly, when excitation occurs exclusively in one semiconductor component, its counterpart functions solely as charge reservoirs. Consequently, type-II heterojunctions achieve enhanced carrier separation at the expense of compromised oxidation/reduction capability. This review examines advancements in PDI-based type-II heterostructure composites.

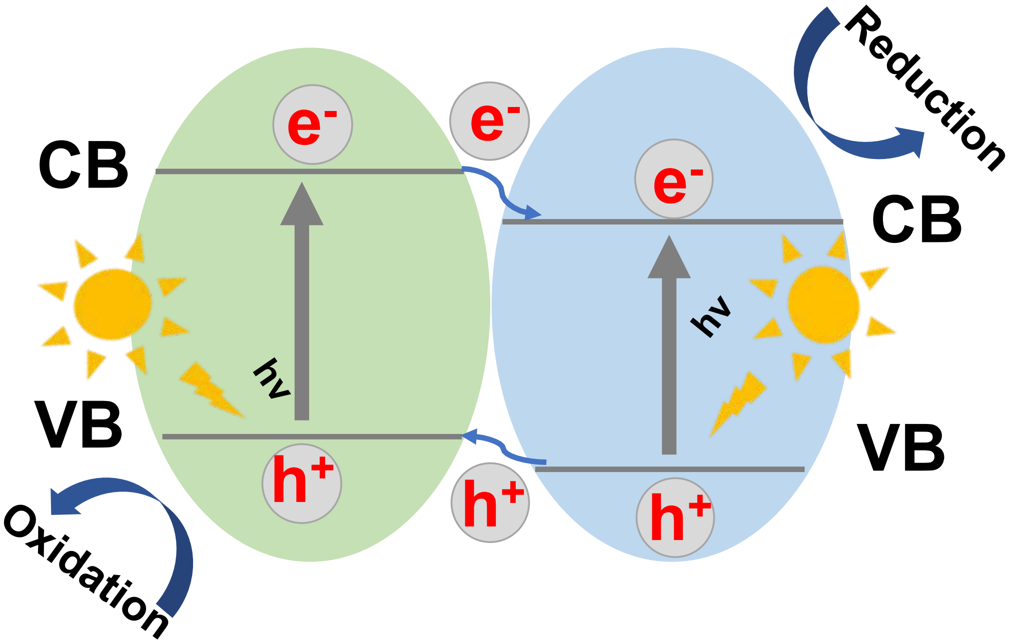

Figure 6. Charge transfer mechanism in type-II heterojunctions.

Bismuth-based photocatalysts have emerged as prominent materials owing to their extended light-harvesting range, modifiable energy band characteristics, and unique electronic properties. However, persistent limitations include inadequate photon capture efficiency and structural instability. A promising strategy to mitigate these constraints involves constructing heterostructures through integration of PDIs with these photocatalytic systems. For instance, Zhang et al.[82] synthesized Bi_2WO_6/PDI heterojunction via water bath heating. Under visible light, Bi_2WO_6/PDI heterojunction exhibited higher phenol degradation rates than pure Bi_2WO_6 or self-assembled PDI, and doubled the oxygen production rate of pure PDI **(Figure 7b-c)**. The enhanced activity stems from the formation of an n-n Type-II heterojunction which staggered band alignment facilitates charge separation **(Figure 7a)**.

Research in photocatalysis shows considerable potential for nonmetallic carbon-based semiconductors due to their superior optoelectronic characteristics and eco-compatibility. Type-II heterojunctions between PDIs and carbon materials have also gained increasing attention for applications. Particularly noteworthy are n-type graphitic carbon nitride (g-C_3N_4) photocatalysts, which represent the most extensively investigated system in this category. Li et al.[83] synthesized a g-C_3N_4/PDI@NH_2-MIL-53(Fe) (CPM) type-II heterojunction via thermal polymerization, surface growth, and solvothermal methods**(Figure 7d)**. The CPM heterojunction demonstrated exceptional visible-light photocatalytic activity with H_2O_2, degrading aqueous pollutants rapidly. This superior performance stems from the optimized type-II heterojunction. Close interfacial contact and aligned band structures between g-C_3N_4/PDI and NH_2-MIL-53(Fe) enhance charge separation.

Ternary or multicomponent systems enhance carrier separation efficiency through synergistic effects. Wang et al.[84] developed a visible-light-responsive BiOBr/$Bi_4O_5Br_2$/PDI dual heterojunction photocatalyst for efficient degradation of endocrine-disrupting chemicals (EDCs) in water **(Figure 7e)**. The aligned energy bands between $Bi_4O_5Br_2$ and BiOBr promote heterojunction formation, improving space-charge separation. Simultaneously, PDI loading extends the photo-response range while facilitating carrier transfer and separation. Within this dual-heterojunction system: (1) Electrons migrate to BiOBr's CB. (2) Holes accumulate on PDI's VB. This charge separation enables H_2O oxidation to O_2 followed by $•O_2^-$ formation through reduction. Notably, photocatalytic activity persists significantly under anoxic conditions.

Metal-organic frameworks (MOFs) constitute porosity-defined crystalline solids formed by metal nodes cross-linked to organic molecular bridges. Their extensive surface exposure, abundant coordination centers, facile surface functionalization, and tunable porosity enable widespread applications in environmental remediation and catalytic processes. Wu et al.[85] successfully modified PDI onto NH_2-MIL-88B(Fe, Mn) (FM88B) via water bath heating, forming a PDI/FM88B type-II heterojunction **(Figure 7f)**. This modification, confirmed by amide bond formation **(Figure 7g)**, enhanced structural stability and created an efficient interfacial electron transfer pathway. In the photo-Fenton system, 6%-PDI/FM88B achieved 89% tetracycline (TC) degradation under 30 min visible light. **(Figure 7h)**. The performance enhancement arises from synergistic photocatalysis-Fenton processes, wherein the type-II heterojunction directs photoinduced electron transfer from PDI (donor) to FM88B (acceptor), while the interfacial IEF crucially promotes e^--h^+ separation and directional migration-further amplified by the heterostructure's strong light absorption.

Despite demonstrating effective photogenerated charge segregation, it still exhibits limitations such as: (1) In Type II heterojunctions, electrons transfer from the CB of the narrow-bandgap semiconductor to the CB of the wide-bandgap semiconductor, while holes migrate from the VB of the wide-bandgap to the VB of the narrow-bandgap semiconductor. This results in preserved carriers with both reduced redox potentials compared to the individual semiconductors. (2) The light absorption range of Type II heterojunctions is fundamentally constrained by the narrow-bandgap component, leading to inefficient broadband solar energy utilization. (3) In Type II heterojunctions formed solely through physical contact, interfacial defects or gaps introduce additional charge-transfer resistance, significantly compromising carrier separation efficiency. (4) The preserved charge carriers with diminished redox potentials tend to accumulate and recombine in the absence of sacrificial agents for hole/electron consumption, ultimately degrading catalytic efficiency. Consequently, the type-II mechanism remains controversial.

View Article Online
DOI: 10.1039/D5MH01487E

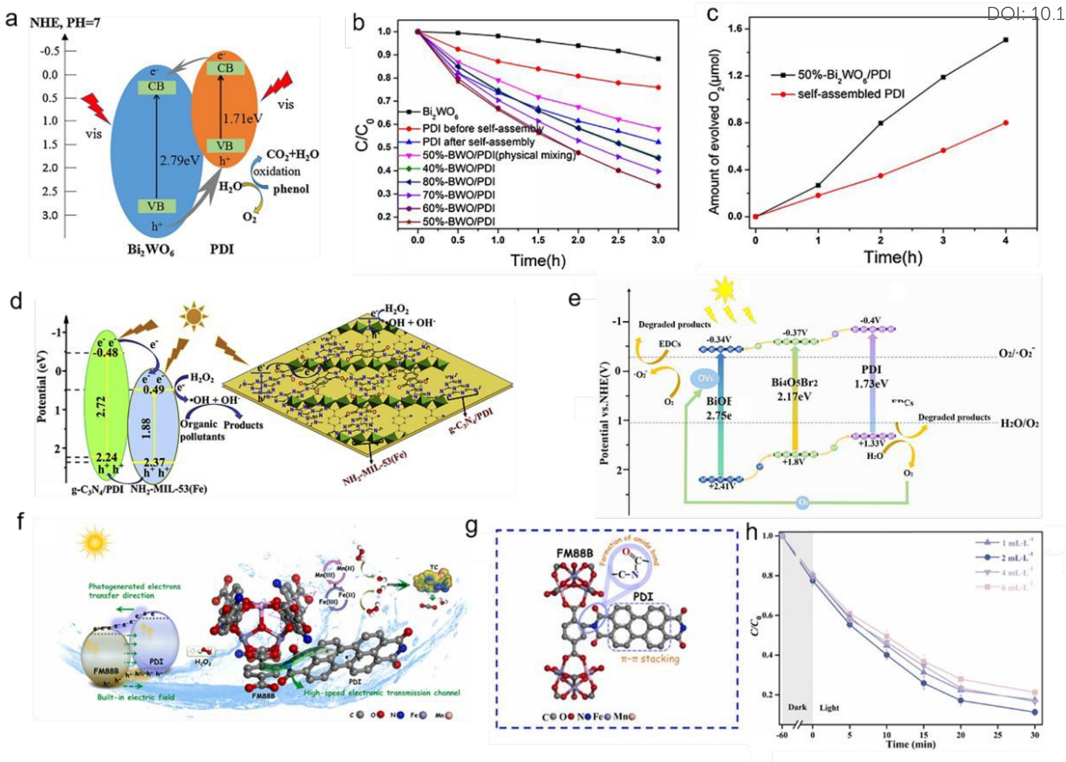

Figure 7. (a) The possible reaction mechanism of Bi_2WO_6/PDI composite materials. (b) Photocatalytic degradation of 5 ppm phenol. (c) Oxygen evolution from water by PDI and 50%-Bi_2WO_6/PDI sample in the presence of an electron acceptor. Reproduced from ref. [82]. Copyright 2018, Elsevier. (d) The possible photocatalytic mechanism of the CPM-2 composite under visible light irradiation. Reproduced from ref. [83]. Copyright 2019, Elsevier. (e) Possible photocatalytic mechanism of the BiOBr/$Bi_4O_5Br_2$/PDI system. Reproduced from ref. [84]. Copyright 2022, Elsevier. (f) Degradation mechanism of TC in the system of visible light/6%PDI/FM88B/H_2O_2. (g) Ammoniation reaction between PDI and FM88B. (h) Effect of H_2O_2 concentration on the degradation efficiency of TC over 6%PDI/FM88B. Reproduced from ref. [85]. Copyright 2024, Elsevier.

3.3.2 PDI-based Z-scheme heterojunction

Z-scheme heterostructures exhibit fundamentally divergent charge transfer pathways compared to type-II configurations. Despite effectively improving carrier separation in these photocatalytic systems, oxidation-reduction processes in constituent semiconductors occur at diminished redox potentials, partially compromising their

View Article Online
DOI: 10.1039/D5MH01487E

inherent redox capacity. Z-scheme photocatalysts have undergone three evolutionary stages of refinement, with Figure 6a illustrating their progression from initial liquid-phase mediators to contemporary direct Z-scheme heterojunctions **(Figure 8a)**.[10, 86, 87] Dating in 1979, Bard et al.[88] proposed the concept of Liquid phase Z-scheme photocatalysis **(Figure 8b)**, which maximizes the redox potential of the heterojunction system, which can not only improve carrier separation, but also maintain strong redox capacity. However, the earliest Z-scheme architecture fundamentally differs from heterojunctions, comprising discrete semiconductor components interconnected by solution-phase redox mediators. This liquid-phase confinement restricts operational applicability, significantly limiting implementation potential. The conceptual foundation for solid-state Z-scheme systems was established by Tada et al. [89] in 2006 **(Figure 8c)**, featuring two photocatalytic materials interlinked via solid electron-shuttling mediators. Upon light irradiation, semiconductors generate electron-hole pairs. In solid-state Z-scheme heterojunctions, electrons from semiconductor B's CB transfer to semiconductor A's VB through electron mediators (e.g., Pt, Au, Ag). This mechanism simultaneously accumulates holes with enhanced oxidation capability in semiconductor B's VB and electrons with heightened reduction capability in semiconductor A's CB. Consequently, spatial separation of photogenerated carriers is achieved while preserving strong redox potential. Furthermore, such solid-state Z-schemes function effectively across solid, liquid, and gaseous environments, significantly expanding their practical applicability.[90, 91] However, achieving directional interfacial electron transfer remains fundamentally challenging. Concurrently, parasitic light absorption by common conductive mediators (e.g., Pt, Au, carbon materials) competes with primary catalytic components, necessitating further optimization of Z-scheme heterojunctions.[89, 92] Based on the first and second generations Z-scheme heterojunctions, direct Z-heterojunctions have been proposed and widely used in photocatalysis **(Figure 8d)**. In 2013 marked the introduction of tertiary-generation mediator-free Z-scheme heterojunctions by Yu et al.[93] comprising dual semiconductor components (PS I and

View Article Online
DOI: 10.1039/D5MH01487E

PS II) with aligned band structures. These form Ohmic interfacial contacts inherently containing defects that serve as recombination centers for PS II's CB electrons and PS I's VB holes. This Ohmic interface inherently contains defects that function as recombination centers for electrons from PS II's CB and holes from PS I's VB. Beyond inheriting advantages of prior Z-scheme generations, direct Z-schemes eliminate solid-state mediators, significantly reducing fabrication costs. Consequently, directional segregation of photoinduced charges is achieved concurrently maintaining robust redox capability.[94] Recent advances extend Z-scheme architectures to PDI supramolecular systems. Constructing such heterojunctions can mitigate fundamental limitations of PDI's insufficiently negative CB potential while preserving its strong oxidative capacity from the more positive VB position.

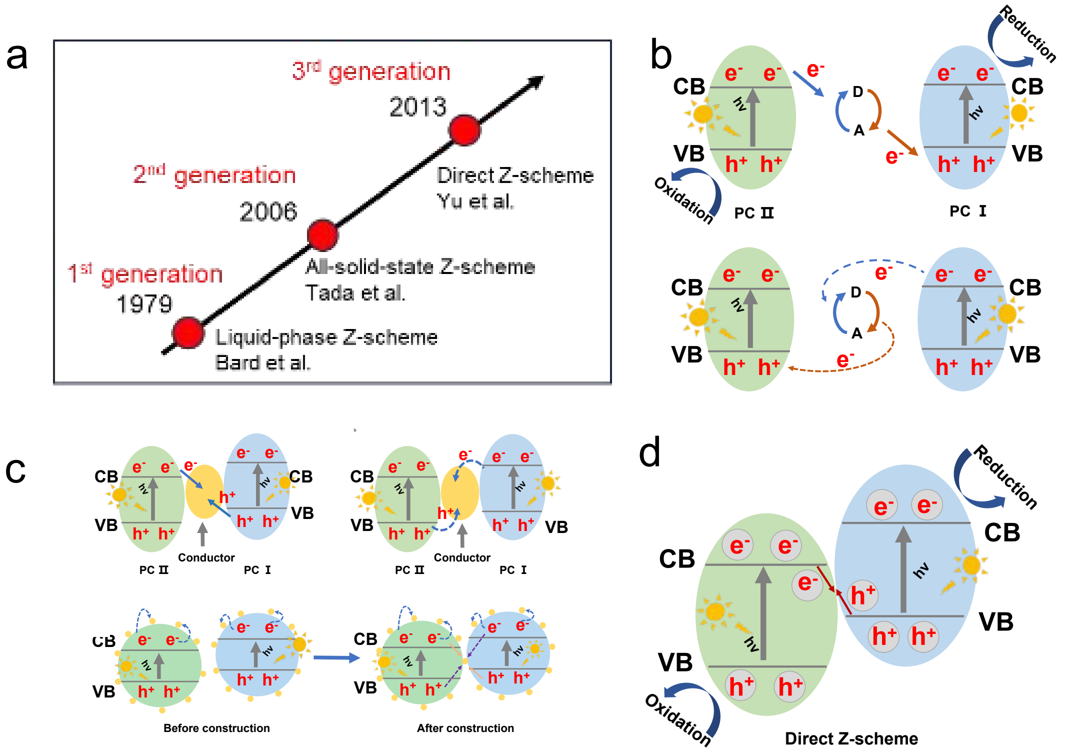

Figure 8. (a) The first generation to the third generation Z-scheme photocatalytic system. (b) Liquid-phase Z-scheme heterojunction. Reproduced from ref. (c) All-solid-state Z-scheme heterojunction. (d) Direct Z-scheme heterojunction.

For example, the π-π stacking in the NDINH/PDINH supramolecular system which developed by Xu et al.[95] creates a giant IEF **(Figure 9a)**, significantly

View Article Online
DOI: 10.1039/D5MH01487E

enhancing charge separation and carrier lifetime. This IEF drives a direct Z-scheme charge transfer pathway, preserving strong redox potentials for both half-reactions. Concurrently, the NDINH coating attenuates backscattered electromagnetic fields across PDINH surfaces, enhancing UV-light utilization efficiency. Exceptional full-spectrum photocatalytic overall water splitting (OWS) activity is enabled by these synergistic effects, achieving H_2 and O_2 evolution rates of 317.2 and 154.8 μmol g^{-1} h^{-1} respectively. This performance is further evidenced by a high O_2 evolution rate of 2.61 μmol g^{-1} h^{-1} (with $AgNO_3$) and 0.13% solar-to-hydrogen efficiency **(Figure 9b-c)**. Dai et al.[96] developed a 3D PANI/PDI direct Z-scheme photocatalytic system. Retained electrons in PANI's CB and holes in PDI's VB drove oxygen radical formation. Meanwhile, a novel PDI/FePc heterojunction featuring strong π-π interactions was synthesized via self-assembled method[97] **(Figure 9d)**. This structure demonstrated enhanced visible-light photocatalytic degradation of tetracycline hydrochloride (TC), achieving removal rates 3-fold and 87.5-fold higher than pristine PDI and FePc, respectively and exhibited superior oxidation kinetics, evidenced by a lower Tafel slope (131.1 mV·dec⁻¹) versus PDI (228.6 mV·dec⁻¹) **(Figure 9e-f)**. The observed boost originates from π-conjugated interactions minimizing layer-to-layer separation within the molecular assembly, consequently enhancing charge separation and transport efficiency.

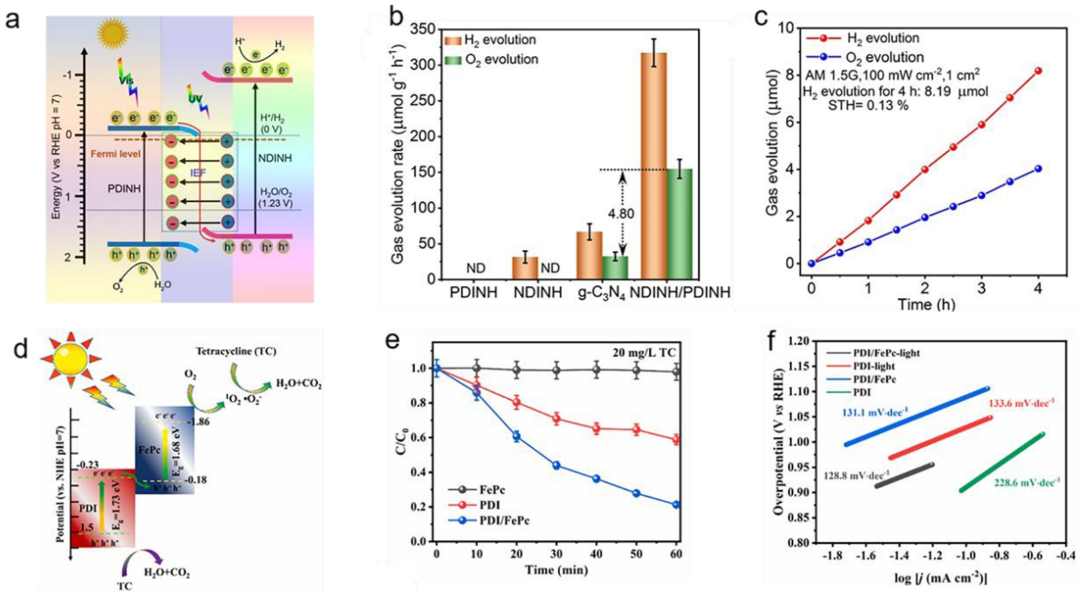

View Article Online
DOI: 10.1039/D5MH01487E

Figure 9. (a) Schematic diagram of NDINH/PDINH Z-scheme electron transfer process. (b) The overall water splitting performance over different catalysts under full-spectrum light irradiation. (c) Time course of photocatalytic overall water splitting over NDINH/PDINH. Reproduced from ref. [95]. Copyright 2023, Wiley. (d) PDI/FePc Z-scheme electron transfer mechanism. (e) Photocatalytic degradation of TC activities over PDI, FePc and PDI/FePc heterojunctions. (f) The corresponding Tafel plots. Reproduced from ref. [97]. Copyright 2023, Elsevier.

3.3.3 PDI-based S-scheme heterojunction

Relative to conventional heterojunctions, Z-scheme architectures significantly enhance spatial segregation of photogenerated electron-hole pairs across distinct semiconductors. However, suboptimal interfacial charge transfer kinetics, compromised redox potentials of charge carriers, and limited photon harvesting efficiency collectively constrain photocatalytic performance enhancement in these systems.[98-100] Furthermore, inherent thermodynamic and kinetic constraints substantially limit the efficiency of conventional Z-scheme heterojunction photocatalysts. To overcome these limitations, the S-scheme (step-type) heterojunction theory was first proposed by Yu et al.[101] pioneered the step-scheme (S-scheme) heterojunction concept, building upon direct Z-scheme architectures. This theoretical framework resolves fundamental ambiguities between traditional type-II and Z-scheme systems while addressing their intrinsic performance barriers. The system comprises two semiconductor materials functioning as a reduction photocatalyst (RP) and an oxidation photocatalyst (OP) respectively, featuring a staggered (type-II) band alignment where both the CB and VB of RP are positioned at higher energy levels than those of OP.[102] Under illumination, both semiconductors generate photogenerated electrons (e^-) and holes (h^+). Driven by the interfacial IEF and band bending, the less reductive electrons in the CB of OP recombine with the less oxidative holes in the VB of RP, while preserving the highly reductive electrons in the CB of RP and the strongly oxidative holes in the VB of OP.[103] This mechanism achieves efficient charge separation while maintaining robust redox capabilities. The Fermi level alignment at the semiconductor junction induces electron migration from the higher-Fermi-level component to the lower-Fermi-level one, establishing an interfacial IEF with vector direction from RP to OP that promotes oriented charge carrier migration. For example, in the ZnTCPP/hBT hybrid system, the carboxyl groups (-COOH) of ZnTCPP form Ti-O-C covalent linkages with surface titanium atoms (Ti) of hBT. This chemical bonding enables intimate interfacial contact and establishes direct charge-transfer pathways between the components (Figure 10).[102] Collectively, three synergistic mechanisms-IEF, band bending, and Coulombic forces-drive selective recombination of OP's CB electrons and RP's VB holes. Consequently, less reactive carriers are eliminated while retaining high-energy electrons in RP's CB and holes in OP's VB for photocatalytic redox reactions.[101] The S-scheme heterojunction thereby achieves:(1) Enhances charge separation and reduces recombination; (2) Maintains strong redox capability and enhances reaction activity; (3) Enhances charge separation efficiency and broadens spectral response; (4) Promotes interfacial stability. These attributes collectively boost photocatalytic activity and solar energy utilization efficiency.

Strategic engineering of electronic band gaps in hybrid organic-inorganic materials through covalent bonding enables precise fabrication of S-scheme heterojunctions. For example, through electrostatic interactions, the modification of PDI with Ag_2S nanoparticles by Yang et al.[104] was confirmed by TEM and HRTEM characterization, revealing uniform dispersion of Ag_2S on PDI surfaces with established heterojunction interfaces **(Fig. 11b)**. The S-scheme Ag_2S/PDI heterojunction **(Fig. 11a)** exhibited superior photocatalytic activity, achieving 94% phenol degradation within 2 hours-significantly outperforming individual Ag_2S or PDI components **(Fig. 11c)**. Owing to its enhanced oxidation capability, the composite also facilitates in situ water oxidation for oxygen evolution. Chen et al.[105] fabricated an organic-inorganic dual S-scheme heterojunction In_2O_3/PDI/In_2S_3 (denoted IO/PDI/IS) photocatalyst through a synergistic approach combining solvent-induced self-assembly and electrostatic

View Article Online
DOI: 10.1039/D5MH01487E

driving forces. The rational design leverages complementary band structures and an intensified IEF **(Fig. 11e)**, enabling a defect-mediated dual S-scheme charge transfer pathway within the IO/PDI/IS architecture **(Fig. 11d)**. This configuration demonstrates exceptional efficacy in degrading recalcitrant organic pollutants, including lignin and antibiotics. Notably, the system achieved an 80.9% mineralization rate for sodium lignosulfonate (SL), highlighting its advanced oxidative capability. Recently, Li et al.[106] developed an organic-inorganic S-scheme heterojunction photocatalyst by incorporating Nb^{5+}-substituted $BiVO_4$ (introducing oxygen vacancies, Ovs) with β-alanine-functionalized PDI supramolecules **(Fig. 11f)**. This strategic modification reduced the bandgap and enhanced visible-light absorption. The composite demonstrated superior degradation efficiency for persistent aquatic pollutants including TC, RhB, SMX, and phenol. The enhanced photocatalytic activity stems from synergistic effects: Ovs facilitate charge separation, while interfacial Nb-O and Bi-O bonds maintain strong redox potentials **(Fig. 11g)**.

In general, hybridizing PDI supramolecular photocatalysts with different semiconductors to form a heterojunction structure has shown to be an effective strategy mainly through extending the light absorption for photo-excitation and reducing the recombination of photo-generated carriers. However, to realize successful and reasonable construction of PDI-based heterojunction, several aspects need to be considered: (1) Matched energy band potentials, allowing effective transfer and spatial separation for charge carriers from one semiconductor to another; (2) Synthetic feasibility, adapt to PDI supramolecular photocatalysts' fabrication condition; (3) Structure and activity stability, essential for their future application.

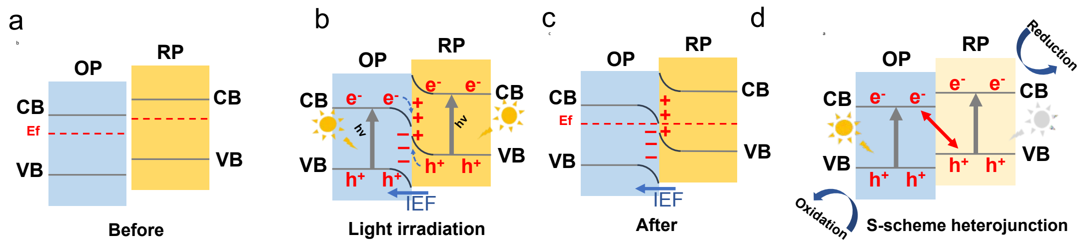

Figure 10. (a-c) Charge-Transfer Processes in an S-Scheme Heterojunction. (a) Schematic illustration of heterojunction with staggered band configuration: (b) before

contact, (c) after contact, photogenerated charge carrier transfer process in S-scheme mode. (d) S-scheme heterojunction.

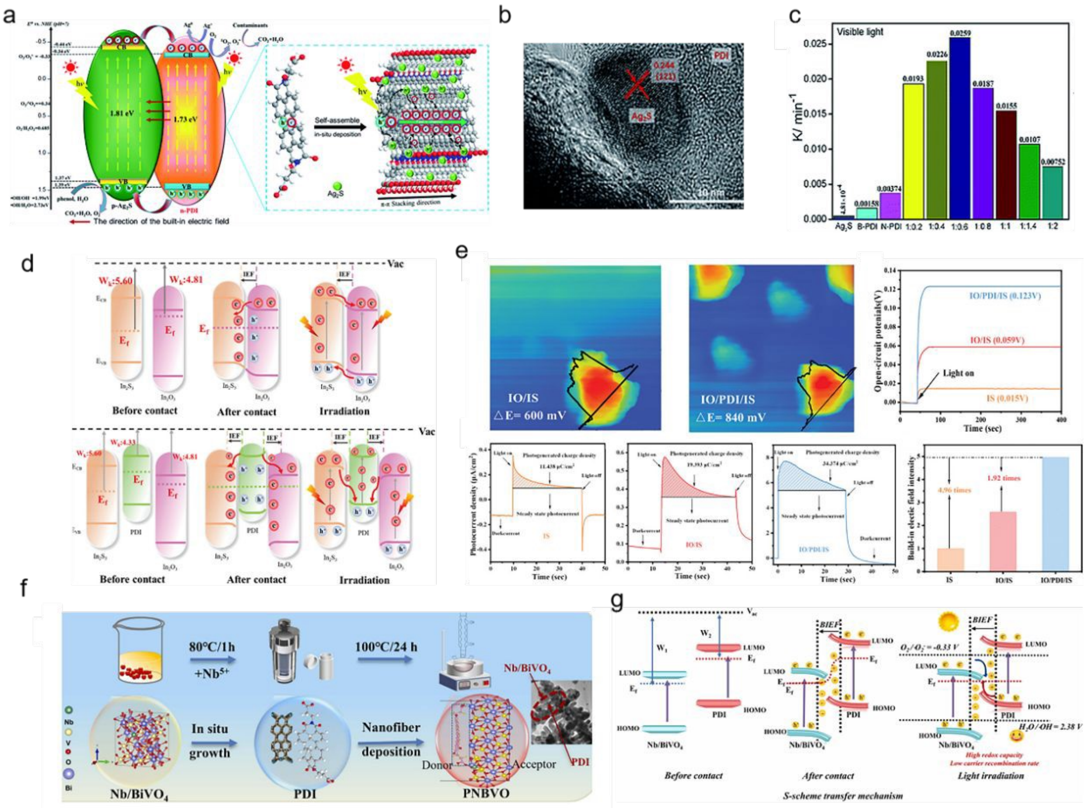

Figure 11. (a)Mechanism of Ag_2S/PDI. (b) The HR-TEM image of Ag_2S/PDI (1:0.6). (c) visible light irradiation (where B-PDI represents bulk-PDI, N-PDI represents nano-PDI, 1:*x* represents the mass ratio of Ag_2S to PDI. Reproduced from ref. [104]. Copyright 2019, the Royal Society of Chemistry. (d) Schematic illustration of the charge migration between IO/IS and IO/PDI/IS. (e) The calculation of IEF intensity of IS, IO/IS and IO/PDI/IS. Reproduced from ref. [105]. Copyright 2023, Wiley. (f) Schematic illustration of the facile solvothermal preparation of PNBVO composite materials. (g) Photocatalytic electron transfer mechanism of PNBVO. Reproduced from ref. [106]. Copyright 2025, Elsevier.

3.4 Metal deposition/doping and co-catalyst engineering

Depositing noble metals onto photocatalysts constitutes an effective approach for enhancing photocatalytic efficiency,[107] primarily through Schottky or Ohmic junction formation that modulates photogenerated charge transfer dynamics. Critically, plasmonic noble metal nanoparticles (e.g., Au, Ag, Cu) exploit localized surface plasmon resonance (LSPR) effects, wherein collective electron oscillations significantly boost photon absorption capacity.[108]

Miao et al.[109] fabricated PDI@Au NPs via electrostatic adsorption, demonstrating enhanced visible-light phenol photodegradation kinetics. This performance enhancement stems from synergistic effects: (1) Au nanoparticle surface plasmon resonance (SPR). (2) Resonance energy transfer (RET) with PDI collectively broadens visible-light utilization; (3) Au's lower Fermi level facilitates efficient electron-hole separation. For another example, Liu's group[110] achieved homogeneous deposition of platinum quantum dots (Pt QDs) on PDI supramolecular nanorods through a facile *in situ* reduction protocol **(Fig. 12a)**. The optimized 1 wt.% Pt QDs/PDI composite exhibited substantially enhanced photocatalytic activity, demonstrating 6.2-fold greater phenol degradation efficiency versus pristine PDI under visible light **(Fig. 12b)**. Critically, the mild synthetic conditions preserved the nanorods' structural and electronic integrity. This performance enhancement stems from Pt QDs functioning as electron-shuttling mediators that efficiently capture and transfer photogenerated electrons, thereby accelerating charge separation kinetics.

Compared to metal deposits, metal doping enables atomic-level dispersion of active sites, preventing deactivation caused by metal particle agglomeration.[111, 112] This strategy significantly increases the mass-specific density of catalytically active sites in the catalyst. For instance, Liang et al.[113] synthesized Cu-doped PDI supramolecules (CuPDIsm) with a 1D structure and integrated them with TiO_2 to form a heterojunction photocatalyst **(Fig. 12c)**. Cu incorporation enhanced visible-light absorption and specific surface area. Crucially, Cu^{2+} coordination bridges and H-type π-π stacking significantly accelerated intramolecular electron transfer within CuPDIsm. Furthermore, photoinduced electrons migrated from CuPDIsm to TiO_2 via interfacial hydrogen bonding and electronic coupling, promoting charge separation. Consequently, the TiO_2/CuPDIsm composite exhibited exceptional visible-light photodegradation activity, achieving 89.87% tetracycline and 97.26%

methylene blue removal **(Fig. 12d-e)**. Recently, Burcu Palas et al.[114] synthesized silver- and cobalt-doped PDI supramolecular photocatalysts and evaluated their efficacy for amoxicillin removal from aqueous solutions. Both bulk PDI and self-assembled PDI (SA-PDI) were functionalized with Ag or Co at 1 wt% and 10 wt% loadings **(Fig. 12f)**. Photocatalytic reaction parameters were optimized at pH 4.6, catalyst loading 0.52 g/L, and initial amoxicillin concentration 10.3 mg/L. Under these visible-light conditions, the optimal system achieved 51.8% amoxicillin degradation efficiency **(Fig. 12g)**.

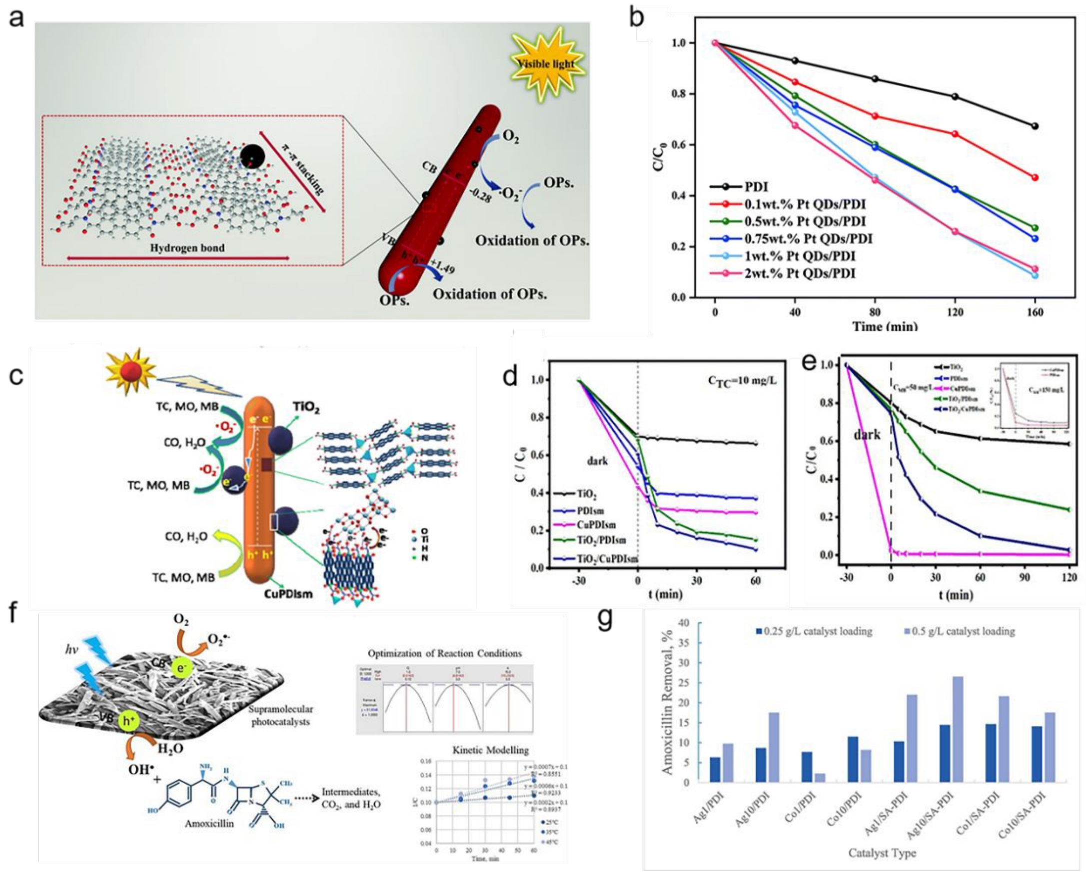

Figure 12. (a) Diagram for the photocatalytic mechanism of Pt QDs/PDI. (b) Photocatalytic degradation performance Pt QDs/PDI composites. Reproduced from ref. [110]. Copyright 2021, the Royal Society of Chemistry. (c) The photocatalytic mechanism of TiO_2/CuPDIsm composite. (d) The photodegradation ratios of the samples toward TC. Reproduced from ref. [113]. Copyright 2023, the Royal Society of Chemistry. (e) The photodegradation ratios of the samples toward MB. (f) The photocatalytic mechanism of SA-PDI composite. (g) Amoxicillin removal

performances of supramolecular catalysts in photocatalytic oxidation. Reproduced from ref. [114]. Copyright 2023, Elsevier.

3.5 Others

The hierarchical organization of PDI supramolecular systems is primarily mediated by π-π stacking, which dictates both structural integrity and optoelectronic properties. Intensified stacking interactions promote long-range π-conjugation and molecular orbital hybridization-key determinants for optimizing charge carrier mobility and separation efficiency in organic semiconductor architectures.[115] Based on the π-π stacking interactions in PDI supramolecular materials, researchers have integrated PDI with complementary π-conjugated organic systems to construct a larger π-π composite system. For example, Wei et al.[95] developed a π-π-stacked NDINH/PDINH supramolecular photocatalyst via rapid solution assembly. The strong intermolecular π-interactions induce a pronounced IEF and efficient charge transport. This optimized π-stacking configuration achieves full-spectrum overall water splitting with H_2/O_2 evolution rates of 317.2/154.8 $\mu mol\cdot g^{-1}\cdot h^{-1}$ and exceptional 32-hour stability, demonstrating the pivotal role of π-π molecular engineering in photocatalyst design. Dai et al.[116] fabricated a 3D PANI/PDI heterojunction photocatalyst via in situ growth. The PANI framework enhances mechanical robustness and provides abundant reactive sites/mass transport pathways. Strong π-π interactions establish an extended delocalized π-system and favorable heterojunction, significantly promoting charge carrier separation. Consequently, tetracycline degradation rates increased 15.3- and 17-fold versus pristine PDI and PANI, respectively, with sustained activity over 75 h in continuous flow.

As a π-conjugated organic component, PDI supramolecular architectures integrate with some other highly π-conjugated material to buildπ-π composite system can enhance interplanar coupling and reduced stacking distances correlate with increased π-electron delocalization and orbital density superposition. These electronic configurations demonstrably facilitate charge carrier migration and separation,

View Article Online
DOI: 10.1039/D5MH01487E

ultimately boosting photocatalytic efficiency and operational stability.

4. Photocatalytic application

Owing to their high stability and narrow band gap, PDIs exhibit strong optical responses across the visible to near-infrared spectrum, enabling their widespread application in photocatalysis such as energy storage, energy conversion, and environmental protection. In this section, we present a succinct overview of their applications in photocatalytic water splitting, CO_2 reduction, N_2 fixation and pollutant degradation.

4.1 Water splitting

Photocatalytic technology plays a significant role in developing green energy and addressing energy and environmental challenges. In recent years, photocatalytic water splitting has attracted increasing attention in the global energy and environmental crisis due to its clean and environmentally friendly characteristics.[100, 117-120] However, the widespread application of conventional inorganic photocatalysts (e.g., TiO_2) is hindered by limitations including poor visible-light utilization, low quantum yield, and high cost.[121] To overcome these constraints, the development of novel, efficient photocatalytic materials is actively pursued. Notably, PDI-based photocatalysts have rapidly emerged as a research focus, particularly for photocatalytic water splitting. Their prominence stems from exceptional light-harvesting capacity, high electron mobility, robust chemical and photochemical stability, and the unique ability to precisely tailor band structures and surface properties through molecular engineering.

4.1.1 H_2 production

The rapid progression of modern society faces major energy challenges due to rising consumption and depleting fossil fuels. Converting abundant solar energy into

View Article Online
DOI: 10.1039/D5MH01487E

chemical fuels like H_2 is therefore of significant interest. Photocatalytic water splitting under sunlight irradiation using a photocatalyst for H_2 production represents an effective approach to addressing energy and environmental issues.[86, 122] Thermodynamically, active photocatalysts require a CB edge more negative than the H^+/H_2 reduction potential (0 V vs. NHE, pH=0) and a VB edge more positive than the O_2/H_2O oxidation potential (1.23 V vs. NHE, pH=0). Most of PDI-based photocatalysts, with a CB around -0.8~-0.1 eV vs. NHE,[62, 123, 124] are thus widely studied for photocatalytic H_2 production. Their H_2 production activities are summarized in **Table 3** for comparison.

However, the photocatalytic H_2 production performance of pure PDIs is severely limited by inherent challenges including unfavorable band structure, rapid charge-carrier recombination, insufficient surface active sites, and mass transfer constraints.[62, 125] To address these limitations, modification strategies such as side chain regulation, elemental doping, and heterojunction construction are commonly employed to significantly enhance its photocatalytic activity.

Constructing heterojunctions is a common strategy to enhance PDI-based photocatalytic hydrogen production. This approach can effectively promote the separation and transfer of photogenerated electron-hole pairs through the IEF formed at the heterojunction interface, reduce the recombination probability of carriers, and extend their lifetime. Additionally, heterojunctions can broaden the light absorption range of PDI-based materials, allowing them to harvest more solar energy and further boost the photocatalytic hydrogen production performance. For example, Zhu and co-workers[126] designed a novel co-assembled material for photocatalytic H_2 production through π-π stacking interactions of TPPS/PDIs organic semiconductors with a D-A interface (**Fig. 13a-b**). The TPPS/PDIs exhibit a remarkable photocatalytic H_2 production rate of 30.36 mmol g^{-1} h^{-1}, attributed to its pronounced IEF that facilitates efficient charge separation and a giant interfacial potential gradient that extends the lifetime of photoexcited carriers. To broaden the absorption spectrum and enhance the separation of photoinduced charges, Yang et al.[104] reported the

View Article Online
DOI: 10.1039/D5MH01487E

fabrication of p-Ag_2S/n-PDIs via a synergistic strategy combining hydrogen bonding, π-π stacking interactions, and a two-step electrostatic self-assembly process **(Fig. 13c)**. Ag_2S enhances π-π orbital overlap in PDI assemblies, facilitating directional photoelectron transport along the 1D π-conjugated pathways. Concurrently, Ag_2S extends visible-light harvesting capacity, thereby promoting photochemical conversion efficiency. Finally, p-Ag_2S/n-PDIs hetero junction shows superior ultraviolet-light, visible-light and full spectrum photocatalytic performance.

In the context of the water splitting reaction mechanism, the suppression of electron-hole recombination emerges as a pivotal factor for enhancing photocatalytic activity. Additionally, both metal and non-metal element doping strategies have been demonstrated to effectively boost the photocatalytic H_2 production performance of PDIs, thereby offering promising avenues for optimizing their catalytic efficiency in energy conversion systems. For example, the metal-doped supramolecular P-PMPDI-Zr [125]exhibited exceptional hydrogen evolution activity under visible light irradiation, achieving a remarkable rate of 50.46 $mmol \cdot g^{-1} \cdot h^{-1}$, which is 4.34 times higher than that of the Zr-free cationic counterpart. Notably, P-PMPDI-Zr maintains substantial photocatalytic activity even at longer wavelengths, demonstrating an apparent quantum yield (AQY) of 11.70% at 630 nm, along with excellent stability. These results highlight that metal doping serves as a facile and effective strategy to broaden the absorption spectrum and enhance charge transfer in supramolecular systems. Furthermore, doping with Co, Ni, and Cu also significantly improves the HER performance compared to pristine P-PMPDI, further validating the universality of this approach. Xu at all.[127] successfully incorporated non-metallic elements N, S, and Se into PDIs (polyimide derivatives), yielding N-APDI, S-APDI, and Se-APDI samples. These heteroatom-annulated PDI supramolecules exhibited a substantially higher H_2 production compared to non-annulated APDI counterparts. Mechanistically, this enhanced photocatalytic activity is attributed to two key factors (**Fig. 13d**). The incorporation of heteroatoms strengthens the molecular dipole moment, thereby intensifying the IEF to facilitate the separation and migration of photogenerated

View Article Online
DOI: 10.1039/D5MH01487E

charge carriers. Simultaneously, heteroatom annulation generates additional active sites that optimize the hydrogen evolution reaction (HER) kinetics, promoting more efficient H_2 production.

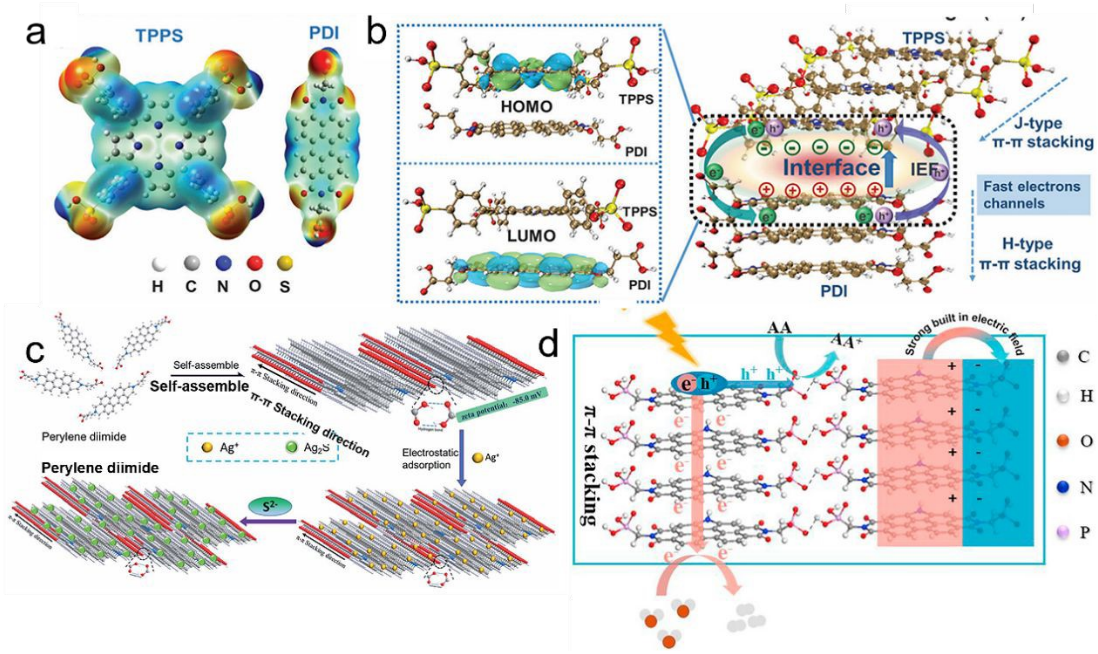

Figure 13. (a) The molecular formula and electrostatic potential distribution of TPPS and PDI. (b) Left: the frontier molecular orbital distribution of TPPS and PDI at the interface; Right: schematic diagram of interfacial interaction of co-assembly supramolecular TPPS/PDI. Reproduced from ref. [126]. Copyright 2022, Wiley. (c) Schematic illustration of the synthesis of the self-assembled PDI and Ag_2S/PDI composite. Reproduced from ref. [104]. Copyright 2019, the Royal Society of Chemistry. (d) Proposed electron transfer mechanism of supramolecular R-APDI for photocatalytic H_2 production. Reproduced from ref. [127]. Copyright 2022, Elsevier.

The fabrication of a PDI heterojunction also presents a dual-pronged advantage: it enhances the efficiency of charge separation and keeps the strong redox capability of photocatalysts, thereby realizing efficient photocatalytic hydrogen generation. For example, Yu and co-workers[128] successfully designed an inorganic-organic S-scheme heterojunction. As illustrated in **Fig. 14a**, ZIS nanosheets are grown onto the disc-shaped MIL-125-PDI surface, forming unique hollow nanodiscs with a hierarchical architecture. This configuration endows the material with abundant surface active sites, a tailored electronic structure, and a spatially segregated redox

View Article Online
DOI: 10.1039/D5MH01487E

interface. Experimental results and theoretical calculations consistently indicate that the staggered band alignment and work function disparity between MIL-125-PDI and ZIS give rise to the formation of an IEF. This electric field, in turn, governs the pathways of charge transfer and consequently improves the efficiency of charge separation (**Fig. 14b**).

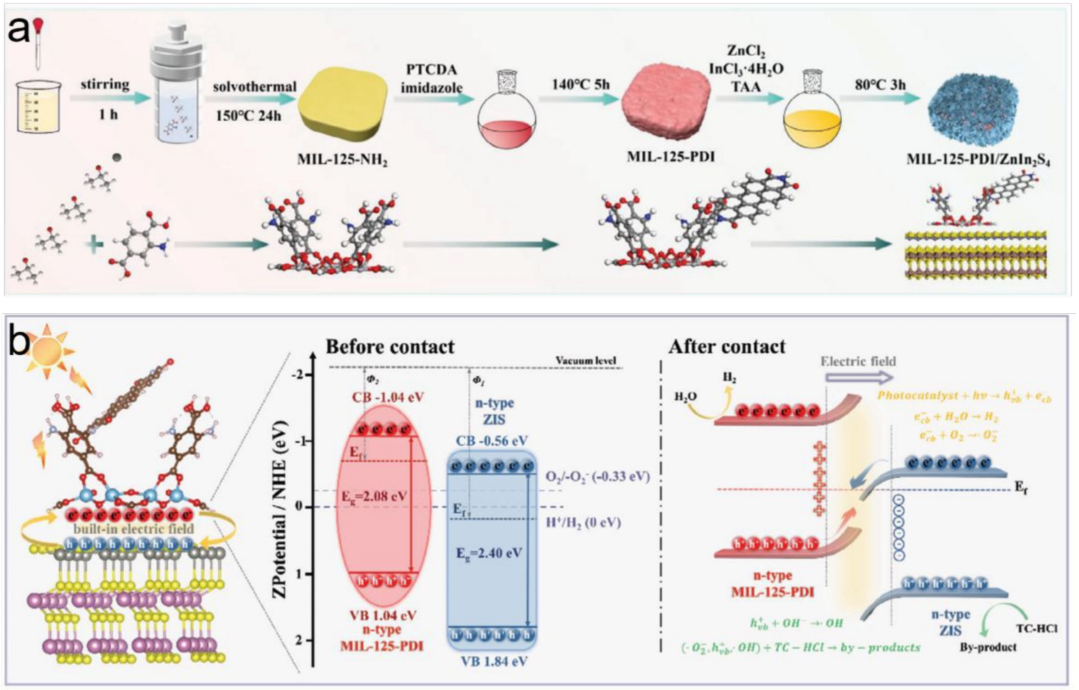

Figure 14. (a) Synthetic route for MIL-125-PDI/ZIS. (b) Schematic of the proposed mechanism of charge transfer over MIL-125-PDI/ZIS under simulated sunlight irradiation. Reproduced from ref. [128]. Copyright 2024, Wiley.

4.1.2 O_2 production

The water oxidation reaction is an essential semi-reaction for photocatalytic water splitting. However, owing to the four-electron transfer reaction, water oxidation becomes the rate-determining step. Photocatalytic water oxidation, a critical half-reaction for overall water splitting, remains a kinetic bottleneck due to its demanding four-electron transfer process. The scarcity of efficient catalysts and inherently slow reaction kinetics impede progress toward large-scale applications. Emerging organic semiconductors-notably graphitic carbon nitride (g-C_3N_4),[129] PDIs,[130] and conjugated organic frameworks (COFs)[131]-offer promise through tunable band structures and thermodynamic feasibility for water splitting. In particular, PDI-based photocatalysts exhibit sufficiently deep VB (+1.6 ~ +2.1 V vs. NHE)[71] to thermodynamically drive water oxidation. However, poor charge separation efficiency limits their oxygen evolution rates. Therefore, the development of PDI photocatalysts with high O_2 production ability is crucial through water splitting. Recent advances in PDI photocatalyst design (e.g., heterojunction engineering, polymer modulation, molecular engineering of PDI monomers and co-catalysts) have significantly improved photocatalytic oxygen production. This section summarizes key developments in high-performance PDI materials for O_2 generation, with comparative metrics detailed in **Table 3**.

Heterojunction engineering represents a key strategy for establishing robust IEFs, which drive directional charge migration to overcome kinetic bottlenecks in photocatalytic O_2 evolution by spatially isolating redox sites. For instance, Yang et al.[104] successfully constructed an efficient full-spectrum responsive p-Ag_2S/n-PDI heterojunction with a photocatalytic O_2 production rate of about 34.6256 mmol g^{-1} h^{-1} **(Figure.15a-b)**. The enhanced photocatalytic performance can be primarily ascribed to several key factors facilitated by Ag_2S: firstly, it optimizes the π-π stacking degree within PDI, significantly improving the mobility of photo-generated electrons along the quasi-one-dimensional stacking channels. Secondly, Ag_2S broadens light absorption, thereby boosting the conversion efficiency of light into chemical energy. Furthermore, the intrinsic IEF formed at the Ag_2S/PDI interface favors the efficient separation of photo-induced charge carriers. This synergistic effect, coupled with the formation of a p-Ag_2S/n-PDI heterojunction, generates a greater quantity of active species compared to pristine PDI, ultimately leading to a substantially enhanced oxidation capability.

Nowadays, enhancing the crystallinity of PDIs during their molecular assembly via non-covalent interactions represents a critical strategy for boosting photocatalytic efficacy. This crystalline ordering facilitates efficient charge carrier transport by augmenting the intrinsic IEF. For example, Zhu et al.[132] synthesized a highly crystalline PDI supramolecular photocatalyst (PDI-NH) via imidazole solvent method **(Figure.15c)**. The catalyst shows a breakthrough oxygen evolution rate with high apparent quantum yield, which is 1353 times higher than the low crystalline PDI-NH **(Figure.15d)**. This crystallinity originates from ordered self-assembly via π-π stacking and hydrogen bonding within the molten imidazole.

PDI supramolecular assembly, held together by weak non-covalent interactions, often suffer from poor structural stability. Therefore, designing PDI polymers is another efficient strategy to improve the O_2 production rate. Liu's group[77] synthesized a high-crystallized linear conjugated polymers Oxamide-PDI, by alternating copolymerization PTCDA with hydrophilic oxamide. The more extended π-conjugation of perylene-cored PTCDA endows Oxamide-PDI with a larger value of interaction energy for π-π stacking. Featuring a planar perylene core with extended conjugation and a polar dicarbonyl bridging group, Oxamide-PDI formed rigid 1D ordered stacks. This structure endowed exceptional π-π stacking-mediated exciton splitting and robust intramolecular charge transfer capabilities through the bridging group. Notably, the highly crystalline Oxamide-PDI achieved remarkable solar-driven O_2 evolution efficiency under mild pH conditions without co-catalysts **(Figure 15e)**.

A notable aspect of the afore mentioned research is its demonstration of efficacy in the absence of oxygen evolution reaction (OER) co-catalysts. Nevertheless, the strategic incorporation of such co-catalysts remains highly advantageous, as they facilitate the extraction and trapping of photogenerated charges, furnish additional redox-active sites, and reduce both the reaction overpotential and activation energy barrier associated with surface oxygen evolution. Consequently, the strategic design of efficient semiconductor/co-catalyst composite materials represents an essential approach for enhancing photocatalytic performance in OER. Li et al.[133] constructed a dual cocatalysts-modified PDI polymer (PDI/Co_3O_4/Pt) for facilitating photocatalytic O_2 evolution performance to improve the solar utilization. The Co_3O_4, acting as superior active sites, contributed to lower the barrier of the water oxidation reaction, and the IEFs of cocatalysts and PDI drive separation and transfer of photogenerated charges. As a consequence, DI/Co_3O_4/Pt exhibited strong stability and a photocatalytic O_2 evolution rate of 24.4 mmol g^{-1} h^{-1}, which is 5.4 times higher than that of pure PDI. The apparent quantum yield of O_2 evolution reaction reaches 6.9% at 420 nm and remains 1.2% at 590 nm. In the system, Co_3O_4 provides the dominant effects for photocatalytic O_2 evolution reactions, and Pt mainly plays a role in charge transfer. **(Figure 15f-g)**.

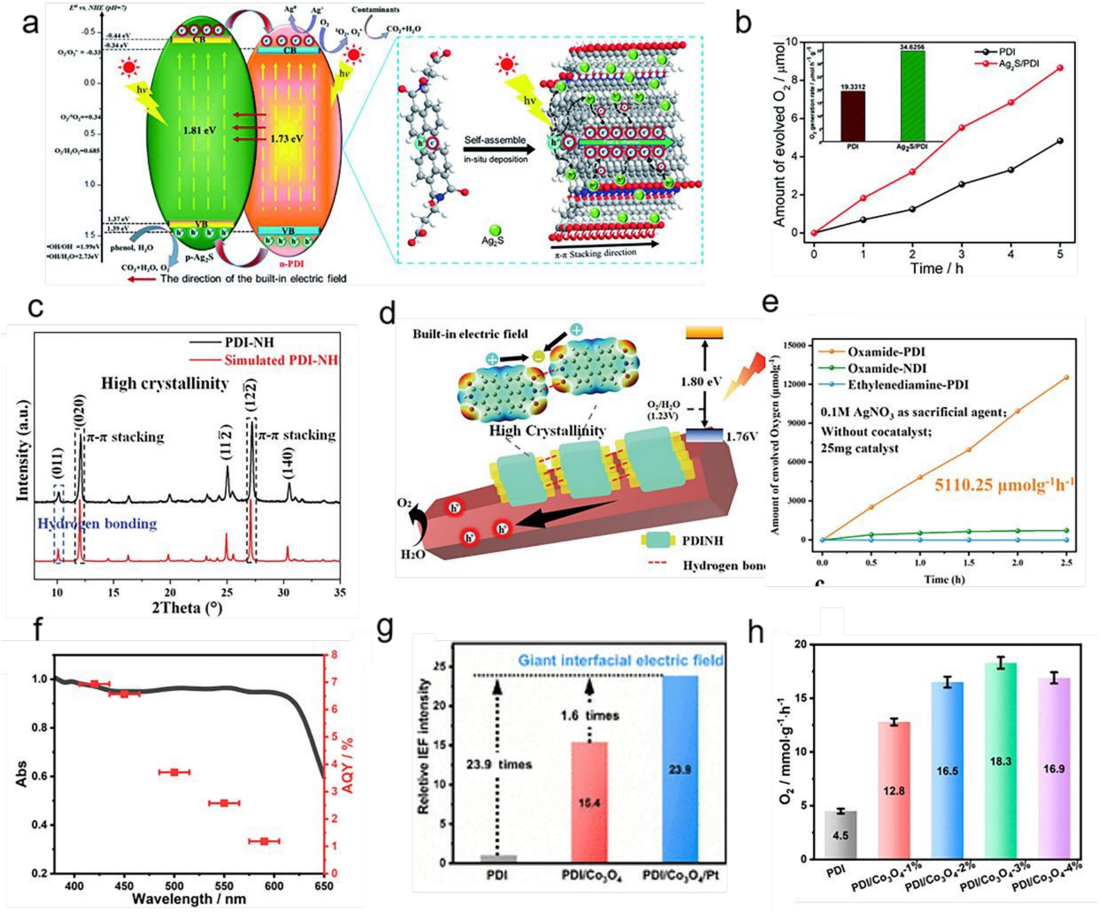

Figure. 15. (a) The synthesis of the self-assembled PDI and Ag_2S/PDI composite. (b) Amount of O_2 evolved of Ag_2S/PDI. Reproduced from ref. [104]. Copyright 2019, the Royal Society of Chemistry. (c) XRD spectrum of PDI-NH. (d) Schematic illustration of PDI-NH. Reproduced from ref.[132] Copyright 2022, Wiley. (e) Amount of O_2 evolved of Oxamide-PDI. Reproduced from ref. [77]. Copyright 2023, Wiley. (f) AQY (g) Relative IEF and (h) Amount of O_2 evolved of PDI/Co_3O_4/Pt. Reproduced from ref. [133]. Copyright 2023, American Chemical Society.

View Article Online
DOI: 10.1039/D5MH01487E

4.2 CO_2 reduction

The photocatalytic conversion of CO_2 and water into chemicals and fuels using light energy, emulating natural photosynthesis, is considered to be among the most promising methods for decreasing atmospheric CO_2 levels.[134-137] Induced photosynthesis via photocatalytic CO_2 reduction reaction (CO_2RR) to value-added chemicals is a long-lasting way to address energy and ecological problems[138-140]. The oxidative half-reaction in photocatalytic systems predominantly involves water oxidation to generate oxygen (O_2) or hydrogen peroxide (H_2O_2). Despite the inherent merits of CO_2 photocatalytic conversion technology, its practical implementation confronts significant challenges. It is still a multi-step process demanding the concurrent fulfilment of both thermodynamic and kinetic criteria. Thermodynamically, the redox potentials of the reaction intermediates must align favorably with the band edge positions of the photocatalyst. Kinetically, the substantial energy barriers associated with multi-electron transfer processes must be overcome. Consequently, an efficient photocatalyst for the overall reduction of CO_2 necessitates both exceptional photogenerated charge separation efficiency and appropriately positioned conduction band minimum and valence band maximum to drive the reduction and oxidation half-reactions, respectively. Therefore, developing highly active photocatalytic systems is crucial for enhancing the reaction rate of photocatalytic CO_2 reduction. Compared to inorganic semiconductors, organic semiconductors offer distinct advantages, including chemically tunable optoelectronic properties, robust photochemical and thermal stability, adjustable band energy levels, flexible morphological and structural design, facile synthetic modulation, and elemental abundance. Among diverse organic semiconductors, PDI exhibits a broad spectral response range, environmental benignity, and low cost, leading to its widespread application in fields such as fluorescent probes, sensors, transistors, and photocatalytic systems.

For example, Hu and co-workers[141] engineered ZrO_2-supported PDI photosensitizers via salicylic acid anchors **(Figure 16a)**. Coupled with

Re(bpy)(CO)$_3$Cl/TEOA in DMF, the composite demonstrated competitive CO_2-to-CO TONs under white LED (100 mW cm^{-2}), attributed to stable surface grafting and facilitated electron transfer at minimal catalyst usage **(Figure 16b-c)**. The strong anchoring of salicylic acid on the surface of ZrO_2 and efficient electron transfer at low catalyst concentrations make ZrO_2/PDIs a promising candidate for CO_2 photoreduction applications.

While the VB position of PDI offers a strong oxidation capability, the positive CB potential results in an insufficient thermodynamic driving force for reduction. Furthermore, rapid recombination of photogenerated charge carriers significantly limits the practical application of PDI. Consequently, PDI-based heterojunction engineering overcomes this limitation through two synergistic mechanisms: (1) tailored energy band alignment and (2) optimized photogenerated carrier separation, ultimately boosting CO_2-to-fuel conversion efficiency when utilizing H_2O as the reductant. For example, Wu et al.[142] fabricated novel 3D MXene/GO/PDI aerogels via self-assembly **(Figure 16d)**, establishing an electron transfer network through π-π stacking that enhanced electron delocalization. The optimized aerogel achieved a formaldehyde (HCHO) production rate of 771.1 μmol g^{-1} h^{-1} in photocatalytic CO_2 reduction an 8-fold enhancement over MXene/PDI **(Figure 16e-f)**. Characterization confirmed a strongly coupled interface via π-π cross-linking, generating a robust IEF and narrowed bandgap. Concurrently, a Z-scheme heterojunction formed between MXene/GO and PDI due to their aligned band structures. This dual configuration accelerated photogenerated electron transfer and enhanced interfacial redox capability.

Non-covalent heterojunctions, characterized by the absence of robust chemical bonding, typically exhibit compromised interfacial carrier transport efficiency. This limitation adversely impacts photocatalytic CO_2 reduction performance. In contrast, covalently bonded heterojunctions feature strong covalent linkages between semiconductor components, providing directional charge transfer channels that enhance photocatalytic activity. Yang et al.[143] constructed Au/PHI-PDI with synergistic junctions: (1) covalent S-scheme heterojunction enabling rapid intralayer charge transfer via PHI-PDI bonds, and (2) Schottky junction creating vertical IEF for interlayer charge transport **(Figure 16g)**. The covalent connection between PHI and PDI constructs a fast charge transfer channel, which is beneficial to boost intralayer charge separation and migration. Furthermore, the formed Schottky junction could generate a vertical IEF, which enhances interlayer charge transport. **(Figure 16h-i)**. As a result, this architecture boosted charge utilization efficiency, yielding 122.65 μmol g^{-1} h^{-1} CO over 3%Au/PHI-PDI surpassing PHI-PDI and PHI by factors of 2.77 and 9.24 respectively.

Currently, the integration of PDI with organic frameworks has also begun to be investigated in the field of photocatalytic CO_2 reduction, such as in metal-organic frameworks (MOFs), covalent organic frameworks (COFs) etc. For example, research on MOFs containing PDI has focused on applications in sensing[144] and photocatalytic degradation,[145, 146] few studies have studied their potential for CO_2 conversion. Recently, Altalbawy and co-workers[147] incorporated a PDI chromophore moiety into a Cu@PDI(30 %)-NZU67 and applied the resulting material for CO_2 conversion of ETHO for the first time **(Figure 16j-l)**. From a MOF engineering perspective, anchoring PDI within secondary building units (SBUs) proved strategically superior to conventional linker-based integration. For another, Zhu and colleagues[148] developed a cobalt-metalated, one-dimensional covalent organic framework with ABC stacking (PP-COF-Co). This framework integrates PDI as a photosensitizing unit and 1,10-phenanthroline moieties as metal-coordinating sites which exhibits a 57-fold increase in photocatalytic CO_2 reduction activity compared to its pristine analogue.

View Article Online
DOI: 10.1039/D5MH01487E

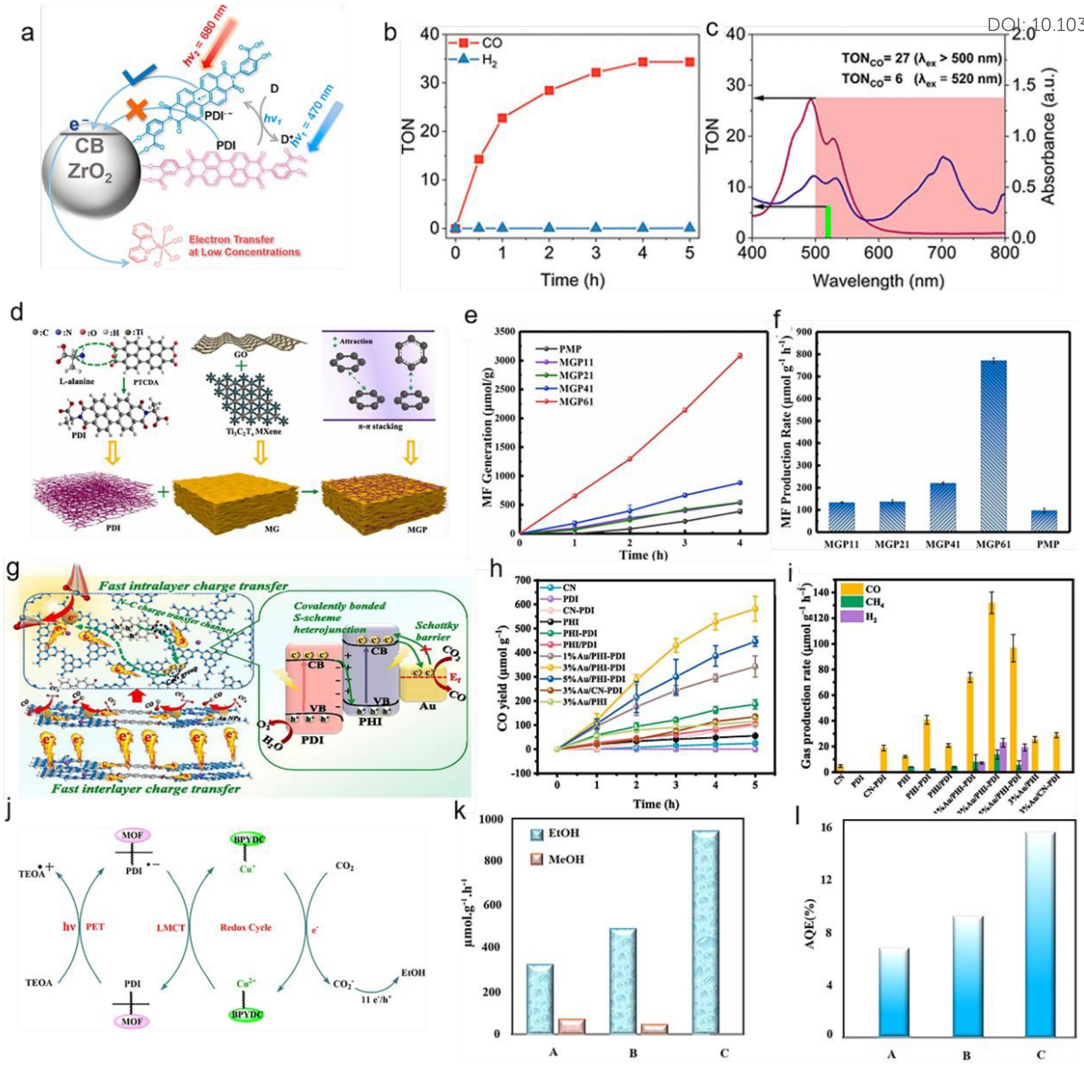

Figure 16. (a) Strategy for Photogeneration of a Potent and Long-Lived $ZrO_2(e^-)$. (b) TON of CO and H_2 by $Re(bpy)(CO)_3Cl$ and $ZrO_2|PDI$ as a function of irradiation time. (c) Photocatalytic CO_2 reduction TON under 520 nm irradiation or broad band irradiation with wavelengths greater than 500 nm. Reproduced from ref. [141]. Copyright 2022, American Chemical Society. (d) Schematic illustration of the MXene/GO/PDI composite aerogels. (e) MF generation yield of samples changing over time under the irradiation for 4 h. (f) MF generation rate of samples under the irradiation for 4 h. Reproduced from ref. [142]. Copyright 2022, Elsevier. (g) Proposed photocatalytic mechanism for Au/PHI-PDI. (h) Time-dependent CO evolution performances. (i) Stability test over the 3%Au/PHI-PDI. Reproduced from ref. [143]. Copyright 2025, Elsevier. (j) Proposed photocatalytic mechanism for Cu@PDI(30%)-NZU67. (k) Photocatalytic activity: Cu@PDI(30 %)-NZU67 (50 mg),

irradiation wavenumber = 420 nm, TEOA (0.3 M), MeCN/deionized H_2O (4:1 v/v). (l) AQE results of Cu@PDI(30 %)-NZU67. Reproduced from ref. [147]. Copyright 2024, Elsevier.

4.3 N_2 fixation

Ammonia (NH_3) serves as an essential industrial chemical for manufacturing explosives and fertilizers, underpinning critical societal infrastructure.[149-151] Conventionally, industrial-scale NH_3 production employs the Haber-Bosch process, where Fe-based catalysts mediate N_2 and H_2 conversion under elevated temperatures and pressures.[152-155] With annual global energy consumption of ~2% and responsibility for 1.6% of anthropogenic CO_2 emissions[156, 157] Photocatalytic nitrogen reduction reaction (PNRR) represents an emerging sustainable alternative to the conventional Haber-Bosch process. However, the exceptionally strong nonpolar N≡N triple bond in N_2 molecules possesses significant challenges for efficient photocatalytic fixation.[158] Furthermore, existing photocatalysts exhibit sluggish charge transfer kinetics, resulting in unsatisfactory N_2 fixation activity. Therefore, developing green and efficient ammonia synthesis technologies is essential for sustainable global development.

PDI represents a prototypical n-type organic semiconductor among diverse organic semiconductor materials, which is famous for its exceptional visible-light absorption capacity and robust chemical stability hold a great potential in photocatalytic N_2 fixation. In the study conducted by Yang and coworkers,[159] notably, the BOPDI photocatalyst achieved an NH_3 production rate of 74.0 μmol g^{-1} h^{-1} without sacrificial agents or cocatalysts, representing an 11-fold enhancement over conventional PDIs. The apparent quantum yield (AQY) for NH_3 generation reached 1.29% under 450 nm monochromatic irradiation. Mechanistic studies attribute this performance to the intensified IEF, which directs electron migration toward embedded catalytic units while localizing photoinduced holes on benzene/perylene moieties **(Figure 17a-c)**. This spatial charge separation creates long-lived

View Article Online
DOI: 10.1039/D5MH01487E

intermediate states: electrons activate N_2 to form NH_3, while holes drive H_2O oxidation to O_2. This work constitutes the first demonstration of PDI-based composites for photocatalytic N_2 fixation to ammonia. For another study, Wang et al.[160] established a facile solution-phase self-assembly strategy to generate IEFs in PDI-triazine-based polymers. **(Figure 17d)**. The optimized PDIMA-2 photocatalyst achieves exceptional nitrogen fixation performance (49.90 $\mu mol \cdot g^{-1} \cdot h^{-1}$) without co-catalysts or sacrificial agents-surpassing pristine PDI by ~10-fold and outperforming carbon materials **(Figure 17e-f)**. Notably, significant NH_3 production persists under 750 nm monochromatic irradiation. Extended near-infrared absorption originates from triazine-PDI π-π stacking-induced LUMO-HOMO orbital overlap. Mechanistic studies reveal the IEF arises from face-to-face molecular dipoles and π-stacking arrangements, dramatically enhancing carrier separation/migration. Recently, Cui and his co-workers [161] constructed Z-scheme PDI/10H-CNv heterojunctions via in-situ condensation. **(Figure 17g)**. Nitrogen vacancies and curled pores in 10H-CNv boosted N_2 adsorption sites, while the enhanced IEF directed electron-hole separation. This synergy achieved 519.2 $\mu mol \cdot g^{-1} \cdot h^{-1}$ NH_3 and 135.9 $\mu mol \cdot g^{-1} \cdot h^{-1}$. **(Figure 17h-i)**.

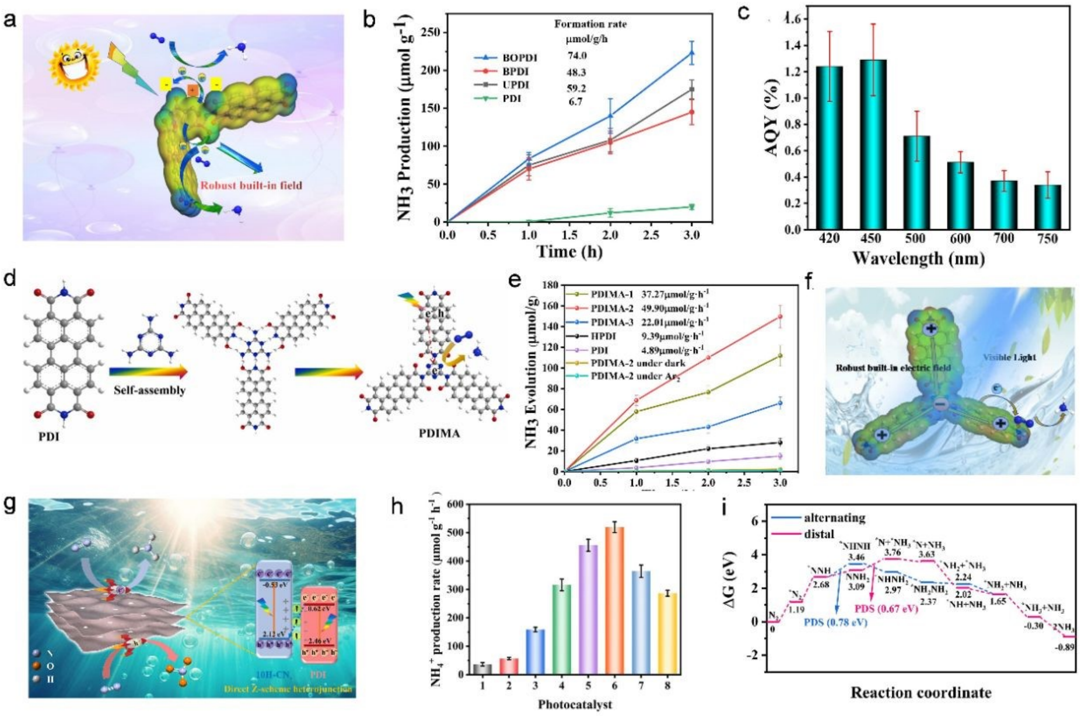

DOI: 10.1039/D5MH01487E

Figure 17. (a) Plausible mechanism for the photocatalytic N_2 fixation over BOPDI under visible light irradiation. (b) NH_3 evolution rates over as prepared BOPDI catalysts. (c) Apparent quantum efficiency (AQY) of BOPDI. Reproduced from ref. [159]. Copyright 2022, Elsevier. (d) Schematic diagram of synthetic route. (e) Ammonia synthesis rates over different samples. (f) Diagram of photocatalytic nitrogen fixation mechanism over PDIMA-2. Reproduced from ref. [160]. Copyright 2022, Elsevier. (g) Direct Z-scheme heterojunction of 10H-CNv. (h) Average NH_4^+ yields for different photocatalysts. (i) Gibbs free energy diagrams of the photocatalytic reduction of ammonia by N_2 in 30 % PDI/10H-CN_v composites. Reproduced from ref. [161]. Copyright 2024, Elsevier.

4.4 Pollutants degradation

Photocatalysis represents a crucial, economical, and effective strategy for addressing environmental pollution.[162-164] Organic semiconductors serve as promising photocatalysts due to their facile synthesis, low cost, tunable functionalization, earth abundance, and robust photochemical stability. PDI, a conventional organic semiconductor widely used in dyes, solar cells, and optoelectronic devices, has recently gained significant attention for photocatalytic applications. In environmental remediation, PDI-based nanocomposites effectively degrade diverse aqueous organic pollutants including antibiotics and phenolic compounds **(Table 3)**. Theoretical calculations reveal PDI’s frontier molecular orbitals: LUMO and HOMO energies derive from carbon and oxygen atomic orbitals, with nitrogen atoms acting as nodal points in π-orbital wavefunctions. Consequently, PDI’s electronic structure primarily depends on π-π stacking interactions.[165] When a PDI-based photocatalyst is excited under illumination， photogenerated electrons in the CB reduce adsorbed O_2 to generate strongly oxidizing superoxide radicals ($\bullet O_2^-$). Simultaneously, VB holes migrate to the material surface, producing hydroxyl radicals (•OH) and directly participating in oxidation. These reactive species ($\bullet O_2^-$, •OH, and h^+) subsequently mineralize organic pollutants into non-toxic inorganic compounds and low-toxicity

View Article Online
DOI: 10.1039/D5MH01487E

small molecules.

Antibiotics and pharmaceutical metabolites accumulating in aquatic environments represent persistent ecological threats due to structural complexity and degradation resistance.[166-169] Conventional water treatment technologies fail to ensure complete elimination. Heterojunction photocatalysts incorporating PDI offer transformative solutions through extended spectral utilization and enhanced carrier separation efficiency. Current advances include strategically designed type-II, Z-scheme, and S-scheme architectures via controlled integration of PDI with complementary semiconductors. Such as g-C_3N_4, metal-organic frameworks, and metal oxides. These designs not only broaden the light absorption range, but also markedly enhance photocatalytic activity through interfacial charge transfer mechanisms. This section systematically reviews the latest advancements in PDI-based heterojunction for the degradation of antibiotics and drug residues, elucidates the underlying mechanisms driving performance enhancement, and explores potential directions for future technological optimization.

For example, an imprinted PDI/PEDOT type-II heterojunction photocatalyst film (I-PDI/PEDOT-M) was engineered via N-methylpyrrolidone (NMP)-induced surface self-corrosion assisted rapid spin-coating[170] **(Figure 18a)**. Under 1 h visible light irradiation, the degradation efficiencies for tetracycline (TC) and ciprofloxacin (CIP) reached 73.7% and 5.0% respectively. Notably, TC degradation efficiency exceeded CIP by 14.65-fold. **(Figure 18b).** This pronounced divergence originates from the type-II heterojunction between PDI and PEDOT, which enables directional carrier separation that sustains superior photocatalytic activity in I-PDI/PEDOT-M. Mao et al.[171] successfully synthesized a PDI/WO_3/α-Fe_2O_3, PWF composite photocatalyst with a dual Z-scheme heterojunction via the pulsed laser ablation in liquid (PLAL) technique **(Figure 18c)**. Photocatalytic performance evaluation revealed that the PWF composite achieved a 94.2% TC removal efficiency under 180 min of irradiation using a 15 W low-pressure mercury lamp (λ = 254 nm) **(Figure 18d)**. The enhanced photocatalytic activity can be primarily attributed to two key factors: (1) Dual

View Article Online
DOI: 10.1039/D5MH01487E

mechanisms drive performance enhancement; (2) augmented adsorption capacity via site density/surface charge optimization; (3) band-engineered dual Z-scheme heterojunction enabling synergistic photoconversion-charge separation efficiency gains.

Besides antibiotics, PDI-based photocatalysts can also be employed for the degradation of phenols. In a related study, through solvent-exchange self-assembly, Zha et al.[172] constructed Z-scheme PDIBr/TiO_2(A10) heterojunctions. The composite demonstrated dual-mode BPA degradation: 71.04% (sacrificial-agent-free) vs 71.7% (persulfate-assisted) under visible light. (**Figure 18e**). The composite demonstrated dual-mode BPA degradation was 71.04% (sacrificial-agent-free) vs 71.7% (persulfate-assisted) under visible light **(Figure 18f)**. Critical enhancement derives from interfacial H-aggregates with π-π orbital overlap that enable directional charge transport and inhibit recombination. Spectroscopic evidence verifies the Z-scheme mechanism as the principal BPA degradation route.

In addition to phenols and antibiotics, PDI-based materials can also be used to degrade other pollutants, such as rhodamine b, methylene blue and methyl orange etc. Zhang et al.[173] successfully fabricated PDI/BiO_2-type-II heterojunctions through ultrasonic-assisted self-assembly technology. The materials exhibited remarkable photocatalytic performance under visible light irradiation, achieving a remarkable degradation efficiency. The key factor behind the enhanced performance was the IEF in type-II heterojunctions, which effectively drives the spatial separation of photogenerated carriers. Zhang et al.[174] achieved efficient synthesis of PDI/Bi_2O_4 type-II heterojunction photocatalysts using water bath heating coupled with ultrasonic dispersion. Remarkably, the 5% PDISA/Bi_2O_4 material degraded 98.6% of RhB and 97.0% of methylene blue within 25 min under visible light. The key mechanism involved an IEF formed at the heterojunction interface, which critically accelerated the separation and migration of photogenerated carriers, leading to superior photocatalytic performance. Furthermore, Xu et al.[175] fabricated a PDISA/AgBr type-II organic-inorganic heterojunctions via chemical co-precipitation. **(Figure 18g)**.

Attributed to synergistic effects of type-II heterojunctions-enhancing photogenerated carrier separation and broadening light absorption-the PDISA/AgBr-40 composite achieved 97.8% RhB degradation in 20 min under visible light **(Figure 18h)**.

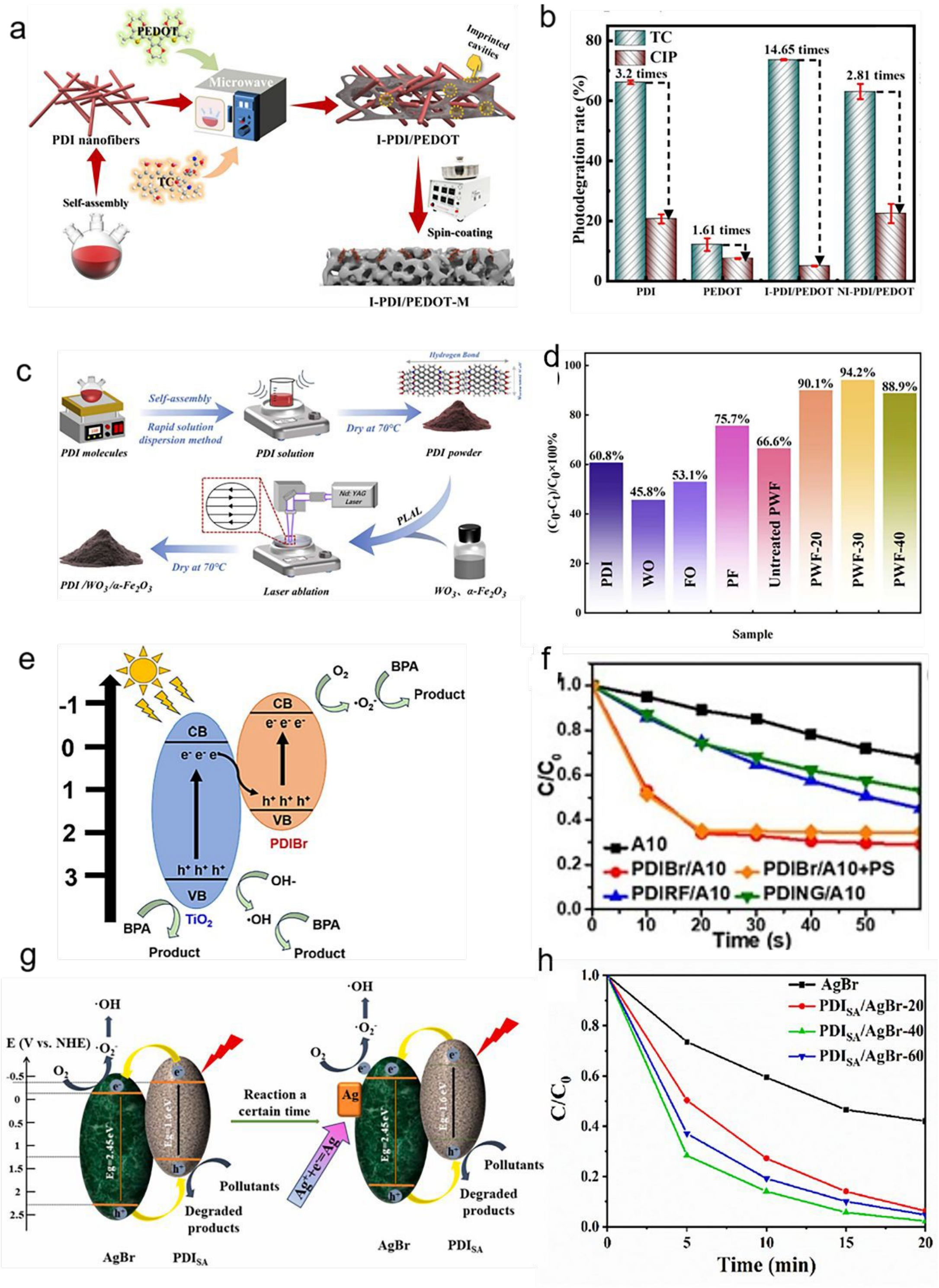

Figure 18. (a) Synthesis process schematic of I-PDI/PEDOT-M. (b) The photodegradation rate of TC and CIP by different powder materials. Reproduced from

View Article Online
DOI: 10.1039/D5MH01487E

ref. [170]. Copyright 2023, Elsevier. (c) Flow chart of pulsed laser preparation of PDI/WO_3/α-Fe_2O_3 composites. (d) Total removal rate of TC in different samples. Reproduced from ref. [171]. Copyright 2025, Elsevier. (e) Schematic illustrations of PDIBr/A10 photocatalytic mechanism. (f) Photodegradation efficiency of A10 base composites about BPA. Reproduced from ref. [172]. Copyright 2024, Elsevier. (g) Photocatalytic degradation mechanism of Rhodamine B over PDI_{SA}/AgBr composite under visible light. (h) Degradation curves of RhB. Reproduced from ref. [175]. Copyright 2024, Elsevier.

Table 3. Summary of the photocatalytic activity of PDI-based photocatalysts.

Photocatalyst	Application	Light source	Amounts of catalysts	Photocatalytic performance	AQY	Re
P-PMPDI	H_2 production	300 W Xe lamp, λ >420nm	50 mg	1170 μmol g^{-1} h^{-1}	2.96 (550 nm)	62
$Zn_{0.5}Cd_{0.5}S$/PDIs	H_2 production	Solar simulator (AM 1.5)	50 mg	1320 μmol g^{-1} h^{-1}	-	124
PDI-phthalic	H_2 production	300 W Xe lamp, λ > 420nm	25 mg	1100 μmol g^{-1} h^{-1}	-	69
N-APDIs	H_2 production	500 W Xe lamp, λ > 420nm	20 mg	61490 μmol g^{-1} h^{-1}	5.9 (420 nm)	127
S-APDIs	H_2 production	Hglamp,500W	20 mg	900 μmol g^{-1} h^{-1}	-	132
g-C_3N_4/PDIs	H_2 production	300 W Xe lamp, λ > 420nm	10 mg	1600 μmol g^{-1} h^{-1}	-	176
TATF-COF/PUP	H_2 production	350 W Xe lamp, λ > 420nm	5 mg	94500 μmol g^{-1} h^{-1}	19.7 (420 nm)	177
GQDs/PDIs	H_2 production	500 W Xe lamp, λ > 420nm	25 mg	1600 μmol g^{-1} h^{-1}	0.5 (420 nm)	178
P-PMPDIs-Zr	H_2 production	300 W Xe lamp, λ > 420nm	50 mg	504600 μmol g^{-1} h^{-1}	11.7 (420 nm)	125
CN-PDI	H_2 production	450 nm LED light source	5 mg	17700 μmol g^{-1} h^{-1}	5.8 (450 nm)	179
TiO_2/PDIs	H_2 production	300 W Xe lamp, λ > 420nm	50 mg	97700 μmol g^{-1} h^{-1}	-	180
g-C_3N_4/Pt/PDIs	H_2 production	400 W Xe lamp, λ > 420nm	25 mg	150 μmol g^{-1} h^{-1}	0.31 (420 nm)	181
PDIs/TiO_2	H_2 production	300 W Xe lamp, λ > 365nm	100 mg	1200 μmol g^{-1} h^{-1}	70.69 (365 nm)	182
PDI-NH	O_2 production	300 W Xe lamp, (420 nm cutoff filter)	15 mg	40.6 mmol g^{-1} h^{-1}	10.4 (400 nm)	132

p-Ag_2S/n-PDI	O_2 production	500 W xenon lamp, 420 nm cut-off filter	25 mg	34 μmol g^{-1} h^{-1}	-	104
Oxamide-PDI	O_2 production	300 W full-spectrum xenon lamp, (783 mW cm^{-2})	0.025 g	5110.25 μmol g^{-1} h^{-1}	2.15 (420 nm)	77
PDI/Co_3O_4/Pt	O_2 production	300 W Xe lamp, 420 nm cut-off filter	15 mg	24.4 mmol g^{-1} h^{-1}	6.9 (420 nm)	133
PT-CB	O_2 production	300 W Xe lamp, (420 nm cut-off filter)	5 mg	966.28 μmol g^{-1} h^{-1}	-	183
3D MXene/GO/PDI	CO_2 reduction	350 W xenon lamp for UV-vis irradiation	10 mg	711 μmol g^{-1} h^{-1} (HCHO)	-	142
3%Au/PHI-PDI	CO_2 reduction	300 W Xe lamp	30 mg	122.65 μmol g^{-1} h^{-1}(CO)	-	143
Cu@PDI(30 %)-NZU67	CO_2 reduction	300 W Xe lamp UV cut-off filter ($\lambda >$ 420 nm)	50 mg	941.28 μmol g^{-1} h^{-1} (ETHO)	-	147
BOPDI	N_2 fixation	300 W Xe lamp ($\lambda > 420$ nm)	20 mg	74 μmol g^{-1} h^{-1}	1.29 (450 nm)	159
PDIMA-2	N_2 fixation	300 W Xe lamp ($\lambda > 400$ nm)	20 mg	49.9 μmol g^{-1} h^{-1}	1.07 (420 nm)	160
30 % PDI/10H-CNv	N_2 fixation	300 W xenon lamp, simulating sunlight (AM 1.5G)	10 mg	519.2 μmol g^{-1} h^{-1}	-	161
3D PANI/PDI	TC removal	5 W LED lamp, (420 nm cut-off filter)	25 mg	0.5265 h^{-1}	-	116
CNPDI	TC removal	250 W xenon lamp, (420 nm cut-off filter)	-	0.026 min^{-1}	-	178
I-PDI/PEDOT-M	TC removal	250 W xenon lamp	20 mg	0.0087 min^{-1}	-	170
FM88B	TC removal	300 W Xenon lamp $\lambda > 420$ nm	7 mg	0.067 min^{-1}	-	85
BN/PDI-2-350	TC removal	visible light, Xenon lamp	15 mg	-	-	184
PDI (5.0%)/BiOCl-$BiPO_4$	RhB/TC removal	visible light irradiation	25 mg	0.037 min^{-1}/0.0135 min^{-1}	-	185
MNP30/PDS/Vis	SMX removal	300 W Xenon lamp, cut-420n m filter	-	0.8873 min^{-1}	-	186
BWGP-2	BPA removal	300 W Xe lamp	-	55%	-	187

5. Conclusions and outlook

This review comprehensively examines recent advancements in enhancing the photocatalytic performance of PDI-based composites through strategic structural engineering and functionalization. Following an analysis of the fundamental molecular architecture and electronic properties of PDI, we discuss several synthetic methods for fabricating PDI-based photocatalysts, correlating their physicochemical properties with performance metrics. Subsequently, we systematically evaluate the deployment of these materials across diverse photocatalytic applications, with particular emphasis on mechanistic insights governing charge transfer pathways. Owing to their tunable band structures and exceptional photostability, PDI-based systems demonstrate significant promise in renewable energy conversion and environmental remediation. Notwithstanding these merits, persistent challenges in carrier recombination kinetics, scalability, and long-term stability necessitate still further investigation to realize their full technological potential. Specifically, as follows:

(1) PDI-based heterojunctions are predominantly assembled through electrostatic assembly, covalent/non-covalent conjugation, or semiconductor surface adsorption. Nevertheless, progressive disruption of interfacial chemical integrity during extended photocatalytic operation compromises charge transfer kinetics and catalytic efficacy. Strategic reinforcement of these interfaces through rational engineering constitutes an essential research priority to ensure operational longevity and practical deployment of PDI heterojunction systems.

(2) Further exploration of PDI's surface/structural properties is essential to optimize its optical and photocatalytic performance. Unique morphologies, exemplified by high-surface-area PDI nanosheets, offer advantages including large specific surface area, reduced charge recombination, and enhanced light utilization. While conventional nanostructures (nanosheets, nanowires, nanorods) are well-understood, high-performance configurations integrating elevated specific surface area with enhanced active site exposure-exemplified by quantum dots, hollow tubes, and hollow spheres-necessitate further exploration.

(3) Current PDI-based composites predominantly absorb visible light, while the

near-infrared (NIR) region (43% of solar spectrum) remains underutilized. Substantial research efforts should therefore focus on developing advanced PDI photocatalysts capable of effective NIR light harvesting to enhance solar energy conversion efficiency.

(4) Advancing the rational design and functional efficacy of PDI-based photocatalysts necessitates a comprehensive mechanistic elucidation of their photocatalytic processes. Beyond fundamental charge carrier dynamics, rigorous investigation into the thermodynamics and microkinetics of surface-mediated catalytic reactions is imperative. State-of-the-art in situ spectroscopic characterization coupled with first-principles computational modelling provides indispensable tools for such fundamental inquiry. These methodologies will unravel critical structure-function relationships, ultimately enabling the precision engineering of PDI-based photocatalysts with exceptional quantum efficiency and reaction specificity.

(5) The established synthetic routes for PDI monomers and polymers remain procedurally intricate, cost-intensive, associated with environmental risks toxic modifiers/solvents, and poor reactor compatibility due to aggregation-induced clogging. To address these challenges, recent advances can employ biocompatible functionalization and solvent-free synthesis to minimize toxicity precluding scalable industrial manufacturing and (e.g., 3D-printed monoliths) to enhance dispersibility. These synergistic strategies achieve cost-effective, environmentally benign (OECD-compliant), and industrially adaptable PDI systems, demonstrating scalable potential for environmental remediation and energy conversion applications.

(6) Current research on PDI supramolecular photocatalysts remains predominantly confined to laboratory-scale investigations. Translational implementation for authentic environmental remediation scenarios merits prioritized exploration.

(7) The growing adoption of additive manufacturing in catalyst engineering enables precise reconfiguration of macroscopic architectures, offering unprecedented control over mass transport and light harvesting dynamics. Integrating 3D printing

technologies with molecularly tailored PDI systems constitutes a promising frontier for designing spatially programmable photocatalysts-where supramolecular organization and reactor geometry synergistically optimize quantum efficiency and scalability.

The future development of PDI-based photocatalysis presents both transformative opportunities and critical challenges. This review establishes a framework for designing high-performance PDI systems, emphasizing four key metrics, i.e., photocatalytic activity, structural stability, reaction selectivity, and visible-light harvesting capacity. Deeper integration of theoretical simulations with experimental validation will accelerate mechanistic understanding and material innovation. With sustained interdisciplinary efforts, PDI-based photocatalysts are poised to enable paradigm-shifting applications in sustainable chemistry.

Author contributions

Initiation and conceptualization: G.L. and P.W. Methodology and formal analysis: Y.X., Z.C., and X.L. Investigation: Y.X., G.D., X.W., and Z.W. Funding acquisition: G.L. Project administration: G.L. Supervision: G.L., and P.W. Writing-original draft: Y.X., Z.C., and X.L. Writing-review and editing: G.L. and P.W.

Acknowledgements

This work was supported by the National Natural Science Foundation of China (Grant No. 52203110), the Youth Talent Support Program of China Association for Science and Technology (Grant No. 2023QNRC0692), and the Natural Science Foundation of Fujian (Grant No. 2024J01403).

Competing interests

The authors declare that they have no competing interests.

References

1. J. Zhang, D. Yan, G. Ding, X. Wang, C. Li, S. Zhong, Y. Yu, L. Shuai and G. Liao, *Angew. Chem. Int. Ed.* 2025, e202511448. DOI: 10.1002/anie.202511448.
2. G. Liao, E. Sun, E. B. G. Kana, H. Huang, I. A. Sanusi, P. Qu, H. Jin, J. Liu and L. Shuai, *Carbohydr. Polym.*, 2024, **341**, 122351.
3. G. Ding, J. Zhang, D. Yan, Y. Yu, L. Shuai, L. Chen and G. Liao, *Nano Lett.*,

DOI: 10.1039/D5MH01487E

2025, **25**, 8984-8992.

4. J. Zhang, Y. Yang, G. Ding, Z. Wang, P. Wang, C. Li and G. Liao, *Chem. Eng. J.*, 2025, **505**, 159165.
5. S. Liu, Y. Guo, S. Yi, S. Yan, C. Ouyang, F. Deng, C. Li, G. Liao and Q. Li, *Sep. Purif. Technol.*, 2023, **307**, 122727.
6. J. Fang, M. Chen, X. Wang, Z. Huang, S. Zhao, P. Wang, Q. Li and G. Liao, *Chem. Eng. J.*, 2025, **516**, 164208.
7. C. Li, G. Ding, P. Wang, K. Liu, B. Yang and G. Liao, *Dalton Trans.*, 2025, **54**, 889-897.
8. Y. Liu, S. Huang, X. Huang and D. Ma, *Mater. Horiz.*, 2024, **11**, 1611-1637.
9. Y. Ahmed, K. R. Dutta, P. Akhtar, M. A. Hossen, M. J. Alam, O. A. Alharbi, H. AlMohamadi and A. W. Mohammad, *Beilstein J. Nanotechnol.*, 2025, **16**, 264-285.
10. C. Li, H. Lu, G. Ding, Q. Li and G. Liao, *Catal. Sci. Technol.*, 2023, **13**, 2877-2898.
11. Z. Wang, G. Ding, J. Zhang, X. Lv, P. Wang, L. Shuai, C. Li, Y. Ni and G. Liao, *Chem. Commun.*, 2024, **60**, 204-207.
12. M. Devaraj and X. Zhou, *Coordin. Chem. Rev.*, 2025, **532**, 216509.
13. G. Liao, Y. He, H. Wang, B. Fang, N. Tsubaki and C. Li, *Device*, 2023, **1**, 100173.
14. A. G. Akerdi, M. Mohsenzadeh, K. Mahmoudian and S. H. Bahrami, *Int. J. Environ. Sci. Technol.*, 2025, **22**, 7317-7352.
15. G. Liao and M. Wu, *The Innovation Energy*, 2024, **1**, 100047.
16. M. Faraji, M. Yousefi, S. Yousefzadeh, M. Zirak, N. Naseri, T. H. Jeon, W. Choi and A. Z. Moshfegh, *Energy Environ. Sci.*, 2019, **12**, 59-95.
17. T. Luo, L. Gilmanova and S. Kaskel, *Coordin. Chem. Rev.*, 2023, **490**, 215210.
18. C. Li, N.-Y. Huang, Y. Yang, Q. Xu and G. Liao, *Coordin. Chem. Rev.*, 2025, **524**, 216292.
19. W. Zhang, C. Shu, H. Cui, Q. Wan, C.-T. Au, B. Yi and H. Yang, *Macromol. Rapid Commun.*, 2023, **44**, 2300012.
20. Y. Guo, B. Liu, J. Zhang, G. Wang, C. Pan, H. Zhao, C. Wang, F. Yu, Y. Dong and Y. Zhu, *Appl. Catal. B: Environ.*, 2024, **340**, 123217.
21. W. Che, C. Sun, Z. Wu, Y. Sun and Q. Shang, *J. Clean. Prod.*, 2024, **453**, 142235.
22. V. Adepu, M. Tathacharya, R. S. Fernandes, A. Tiwari, S. Siraj, S. Kanungo, N. Dey and P. Sahatiya, *Adv. Mater. Technol.*, 2023, **8**, 2201633.
23. N. Fabre, T. Fukaminato, I. Ikariko, L. Chocron, A. Brosseau and R. Métivier, *Adv. Opt. Mater.*, 2024, **12**, 2400452.
24. Y. Ma, C. Hao, Z. Ning, F. Zhang, J. Cui, T. Jiang and Z. Shi, *Inorg. Chem. Commun.*, 2024, **166**, 112694.
25. Y. H. Koo, Y. Tsutsui, M. Omoto, Y. Yomogida, K. Yanagi, Y. K. Kato, M. A. Hermosilla-Palacios, J. L. Blackburn and S. Seki, *J. Phys. Chem. Lett.*, 2025, **16**, 3232-3239.

26. D. Powell and L. Whittaker-Brooks, *Mater. Horiz.*, 2022, **9**, 2026-2052.
27. F. Brust, O. Nagler, K. Shoyama, M. Stolte and F. Würthner, *Adv. Opt. Mater.*, 2023, **11**, 2202676.
28. R. Gerdes, D. Wöhrle, W. Spiller, G. Schneider, G. Schnurpfeil and G. Schulz-Ekloff, *J. Photochem. Photobiol. A: Chem.*, 1997, **111**, 65-74.
29. Y. Xiao, G. Ding, J. Tao, Z. Wang, Z. Chen, L. Chen, L. Shuai and G. Liao, *Nat. Commun.*, 2025, **16**, 7476.
30. H. Li, C. Wang, X. Bai, X. Wang, B. Sun, D. Li, L. Zhao, R. Zong and D. Hao, *Mater. Chem. Front.*, 2020, **4**, 2673-2687.
31. Q. Zhang, L. Jiang, J. Wang, Y. Zhu, Y. Pu and W. Dai, *Appl. Catal. B: Environ.*, 2020, **277**, 119122.
32. B. Yang, L. Lu, S. Liu, W. Cheng, H. Liu, C. Huang, X. Meng, R. D. Rodriguez and X. Jia, *J. Mater. Chem. A*, 2024, **12**, 3807-3843.
33. Y. Sun, D. Wang and Y. Zhu, *Chem. Eng. J.*, 2022, **438**, 135667.
34. Z. Wang, Q. Peng, X. Huang, Q. Ma, J. Shao and Q. Shen, *Dyes Pigments*, 2021, **185**, 108877.
35. J. Tan, G. Zhang, C. Ge, J. Liu, L. Zhou, C. Liu, X. Gao, A. Narita, Y. Zou and Y. Hu, *Org. Lett.*, 2022, **24**, 2414-2419.
36. S. Chen, P. Slattum, C. Wang and L. Zang, *Chem. Rev.*, 2015, **115**, 11967-11998.
37. C. Huang, S. Barlow and S. R. Marder, *J. Org. Chem.*, 2011, **76**, 2386-2407.
38. D. Liu, J. Wang, X. Bai, R. Zong and Y. Zhu, *Adv. Mater.*, 2016, **28**, 7284-7290.
39. J. Wang, W. Shi, D. Liu, Z. Zhang, Y. Zhu and D. Wang, *Appl. Catal. B: Environ.*, 2017, **202**, 289-297.
40. F. Würthner, C. R. Saha-Möller, B. Fimmel, S. Ogi, P. Leowanawat and D. Schmidt, *Chem. Rev.*, 2016, **116**, 962-1052.
41. J. Wang, D. Liu, Y. Zhu, S. Zhou and S. Guan, *Appl. Catal. B: Environ.*, 2018, **231**, 251-261.
42. M. Más-Montoya and R. A. J. Janssen, *Adv. Funct. Mater.,* 2017, **27**, 1605779.
43. B. Wei, H. Li, H. Chu, H. Dong, Y. Zhang, C.-L. Sun and Y. Li, *Langmuir*, 2024, **40**, 6493-6505.
44. H. Wu, L. Xue, Y. Shi, Y. Chen and X. Li, *Langmuir*, 2011, **27**, 3074-3082.
45. Y. Xu, X. Zhu, H. Yan, P. Wang, M. Song, C. Ma, Z. Chen, J. Chu, X. Liu and Z. Lu, *Chinese J. Catal.*, 2022, **43**, 1111-1122.
46. X. Yang, S. Zhang, P. Li, S. Gao and R. Cao, *J. Mater. Chem. A*, 2020, **8**, 20897-20924.
47. H. Langhals, S. Demmig and T. Potrawa, *Journal für Praktische Chemie*, 1991, **333**, 733-748.
48. S. Tatemichi, M. Ichikawa, T. Koyama and Y. Taniguchi, *Appl. Phys. Lett.*, 2006, **89**, 112108.
49. Y. Liu, M. D. Cole, Y. Jiang, P. Y. Kim, D. Nordlund, T. Emrick and T. P. Russell, *Adv. Mater.*, 2018, **30**, 1705976.

50. Y.-J. Kim, Y. Lee, K. Park, C. W. Ahn, H.-T. Jung and H.-J. Jeon, *J. Phys. Chem. Lett.*, 2020, **11**, 3934-3940.
51. R. Guan, X. Cheng, Y. Chen, Z. Wu, Z. Zhao, Q. Shang, Y. Sun and Z. Sun, *Nano Res.*, 2023, **16**, 10770-10778.
52. S. Ghosh, X.-Q. Li, V. Stepanenko and F. Würthner, *Chem. Eur. J.*, 2008, **14**, 11343-11357.
53. M. E. Ozser, *Mater. Today Commun.*, 2021, **27**, 102446.
54. S. Izawa, K. Uchida, M. Nakamura, K. Fujimoto, J. Roudin, J.-H. Lee, T. Inuzuka, T. Nakamura, M. Sakamoto, Y. Nakayama, M. Hiramoto and M. Takahashi, *Chem. Eur. J.*, 2021, **27**, 14081-14091.
55. Z. Li, J. Jiao, W. Fu, K. Gao, X. Peng, Z. Wang, H. Zhuo, C. Yang, M. Yang, G. Chang, L. Yang, X. Zheng, Y. Yan, F. Chen, M. Zhang, Z. Meng and X. Shang, *Angew. Chem. Int. Ed.*, 2024, **63**, e202412977.
56. W. Liu, C. He, S. Huang, K. Zhang, W. Zhu, L. Liu, Z. Zhang, E. Zhu, Y. Chen, C. Chen and Y. Zhu, *Angew. Chem. Int. Ed.*, 2023, **62**, e202304773.
57. Y. Pu, F. Bao, D. Wang, X. Zhang, Z. Guo, X. Chen, Y. Wei, J. Wang and Q. Zhang, *J. Environ. Chem. Eng.*, 2022, **10**, 107123.
58. R. Yan, M. Song, P. Chen, H. Song, C. Fu, H. Peng and S.-F. Yin, *J. Colloid Interface Sci.*, 2023, **651**, 68-75.
59. L. Zeng, T. Liu, C. He, D. Shi, F. Zhang and C. Duan, *J. Am. Chem. Soc.*, 2016, **138**, 3958-3961.
60. X. Gao, K. Gao, X. Li, Y. Shang and F. Fu, *Catal. Sci. Technol.*, 2020, **10**, 372-381.
61. Y. Guo, B. Liu, J. Zhang, C. Wang, G. Wang, C. Pan, H. Zhao, Y. Dong and Y. Zhu, *Appl. Catal. B: Environ. Energy*, 2024, **350**, 123915.
62. K. Kong, S. Zhang, Y. Chu, Y. Hu, F. Yu, H. Ye, H. Ding and J. Hua, *Chem. Commun.*, 2019, **55**, 8090-8093.
63. T. Weil, T. Vosch, J. Hofkens, K. Peneva and K. Müllen, *Angew. Chem. Int. Ed.*, 2010, **49**, 9068-9093.
64. T. T. Clikeman, E. V. Bukovsky, X.-B. Wang, Y.-S. Chen, G. Rumbles, S. H. Strauss and O. V. Boltalina, *Eur. J. Org. Chem.*, 2015, **2015**, 6641-6654.
65. F. Zhang, Y. Ma, Y. Chi, H. Yu, Y. Li, T. Jiang, X. Wei and J. Shi, *Sci. Rep.*, 2018, **8**, 8208.
66. B. Zhang, S. Wang, S. Min, K. Li, L. Kang and W. Lin, *Mol. Catal.*, 2024, **560**, 114116.
67. M.-H. Lin, M.-H. Fang, Q. Liao and M.-J. Lin, *Dyes Pigments*, 2023, **220**, 111730.
68. Y. Zhang, D. Wang, W. Liu, Y. Lou, Y. Zhang, Y. Dong, J. Xu, C. Pan and Y. Zhu, *Appl. Catal. B: Environ.*, 2022, **300**, 120762.
69. Y. Sheng, W. Li, Y. Zhu and L. Zhang, *Appl. Catal. B: Environ..*, 2021, **298**, 120585.
70. M. Gryszel, T. Schlossarek, F. Würthner, M. Natali and E. D. Głowacki, *ChemPhotoChem*, 2023, **7**, e202300070.
71. Z. Zhang, X. Chen, H. Zhang, W. Liu, W. Zhu and Y. Zhu, *Adv. Mater.,* 2020,

32, 1907746.

72. A. Cao, R. Li, X. Xu, W. Huang, Y. He, J. Li, M. Sun, X. Chen and L. Kang, *Appl. Catal. B: Environ.*, 2022, **309**, 121293.
73. X. Wu, B. Hu, D. Li, B. Chen, Y. Huang, Z. Xie, L. Li, N. Shen, F. Yang, W. Shi, M. Chen and Y. Zhu, *Angew. Chem. Int. Ed.*, 2023, **62**, e202313787.
74. S. Huang, H. Zhang, W. Li, L. Liu, J. Xu, M. Chong, J. Li and Y. Zhu, *Appl. Catal. B: Enviro. Energy*, 2024, **347**, 123790.
75. C. Huang, W. Yu, N. Fang, C. He, Y. Chu and B. Lai, *Sep. Purif. Technol.*, 2025, **360**, 131146.
76. Y.-J. Chen, J.-Z. Zhang, Z.-X. Wu, Y.-X. Qiao, L. Zheng, F. Wondu Dagnaw, Q.-X. Tong and J.-X. Jian, *Angew. Chem. Int. Ed.*, 2024, **63**, e202318224.
77. D. Liu, X. Yang, P. Chen, X. Zhang, G. Chen, Q. Guo, H. Hou and Y. Li, *Adv. Mater.*, 2023, **35**, 2300655.
78. L. Yang, Y. Fu, F. Sun, M. Deng, C. Zhang, N. Li, D. Hao, Q. Wang and G. Zhuang, *J. Colloid Interface Sci.*, 2023, **639**, 472-483.
79. H. Wang, L. Zhang, Z. Chen, J. Hu, S. Li, Z. Wang, J. Liu and X. Wang, *Chem. Soc. Rev.*, 2014, **43**, 5234-5244.
80. Y.-P. Yuan, L.-W. Ruan, J. Barber, S. C. Joachim Loo and C. Xue, *Energy Environ. Sci.*, 2014, **7**, 3934-3951.
81. S. J. A. Moniz, S. A. Shevlin, D. J. Martin, Z.-X. Guo and J. Tang, *Energy Environ. Sci.*, 2015, **8**, 731-759.
82. K. Zhang, J. Wang, W. Jiang, W. Yao, H. Yang and Y. Zhu, *Appl. Catal. B: Environ.*, 2018, **232**, 175-181.
83. Y. Li, Y. Fang, Z. Cao, N. Li, D. Chen, Q. Xu and J. Lu, *Appl. Catal. B: Environ.*, 2019, **250**, 150-162.
84. H. Wang, Y. Zhou, J. Wang, A. Li and P. François-Xavier Corvini, *Chem. Eng. J.*, 2022, **433**, 133622.
85. M. Wu, H. Yang, Q. Wu, Z. He and S. Wang, *J. Environ. Chem. Eng.*, 2024, **12**, 112246.
86. G. Liao, C. Li, X. Li and B. Fang, *Cell Rep. Phys. Sci.*, 2021, **2**, 100355.
87. H. Zhu, C. Zhang, K. Xie, X. Li and G. Liao, *Chem. Eng. J.*, 2023, **453**, 139775.
88. C. D. Jaeger and A. J. Bard, *J. Phys. Chem.*, 1979, **83**, 3146-3152.
89. H. Tada, T. Mitsui, T. Kiyonaga, T. Akita and K. Tanaka, *Nat. Mater.*, 2006, **5**, 782-786.
90. Q. Huang, Q. Zhang, S. Yuan, Y. Zhang and M. Zhang, *Appl. Surf. Sci.*, 2015, **353**, 949-957.
91. J. Yu, S. Wang, J. Low and W. Xiao, *Phys. Chem. Chem. Phys.*, 2013, **15**, 16883-16890.
92. Y. Yuan, R.-t. Guo, L.-f. Hong, X.-y. Ji, Z.-d. Lin, Z.-s. Li and W.-g. Pan, *Mater. Today Energy*, 2021, **21**, 100829.
93. P. Zhou, J. Yu and M. Jaroniec, *Adv. Mater.*, 2014, **26**, 4920-4935.
94. G. Zhang, Z. Wang and J. Wu, *Nanoscale*, 2021, **13**, 4359-4389.
95. X. Xu, L. Meng, J. Zhang, S. Yang, C. Sun, H. Li, J. Li and Y. Zhu, *Angew.*

Chem. Int. Ed., 2024, **63**, e202308597.

96. W. Dai, L. Jiang, J. Wang, Y. Pu, Y. Zhu, Y. Wang and B. Xiao, *Chem. Eng. J.*, 2020, **397**, 125476.
97. K. Shi, M. Zhou, F. Wang, X. Li, W. Huang, K. Lu, K. Yang and C. Yu, *Chemosphere*, 2023, **329**, 138617.
98. C. Li, B. Cheng, J. Shen, H. Wang, M. Yi, P. Gu, R. Liu, G. Liao and Z. Jiang, *Sep. Purif. Technol.*, 2025, **360**, 131116.
99. S. Liu, Y. Zhang, Y. Guo, Z. Cheng, M. Yuan, Z. Xu, G. Liao and Q. Li, *J. Colloid Interface Sci.*, 2025, **686**, 45-62.
100. C. Li, H. Lu, G. Ding, T. Ma, S. Liu, L. Zhang and G. Liao, *Chinese J. Catal.*, 2024, **65**, 174-184.
101. J. Low, J. Yu, M. Jaroniec, S. Wageh and A. A. Al-Ghamdi, *Adv. Mater.*, 2017, **29**, 1601694.
102. J. Wei, G. Zhang, S. Xie, Z. Zhang, T. Gao, M. Zhang and X. Li, *Angew. Chem. Int. Ed.*, 2025, **64**, e202500441.
103. F. Wu, Y. Tang, Y. Pan, J. Han, W. Xing, J. Zhang, G. Wu and Y. Huang, *Small*, 2025, 2500670. DOI: 10.1002/smll.202500670.
104. J. Yang, H. Miao, W. Li, H. Li and Y. Zhu, *J. Mater. Chem. A*, 2019, **7**, 6482-6490.
105. R. Chen, H. Lou, Y. Pang, D. Yang and X. Qiu, *Small*, 2024, **20**, 2306354.
106. N. Li, Y. Niu, W. An, F. Ruan, H. Wu, B. Hui, Y. Wang and G. Fan, *Appl. Catal. B: Environ. Energy*, 2025, **369**, 125141.
107. F. Zhang, H. Peng, S. Jiang, C. Wang, X. Xu and L. Wang, *Environ. Sci. Poll. Res.*, 2019, **26**, 8226-8236.
108. S. Linic, P. Christopher and D. B. Ingram, *Nat. Mater.*, 2011, **10**, 911-921.
109. H. Miao, J. Yang, Y. Wei, W. Li and Y. Zhu, *Appl. Catal. B: Environ.*, 2018, **239**, 61-67.
110. D. Liu, L. Chen, W. Chen, M. Qin and S. Wei, *Dalton Trans.*, 2021, **50**, 4008-4016.
111. B. Yang, L. Lu, Q. Zhang, G. Ding, G. Liao, M. Zhang, X. Liu, R. D. Rodriguez and X. Jia, *Chem. Eng. J.*, 2025, **509**, 161236.
112. C. Li, X. Liu, G. Ding, P. Huo, Y. Yan, Y. Yan and G. Liao, *Inorg. Chem.*, 2022, **61**, 4681-4689.
113. Y. Liang, W. Gui, Z. Yang, K. Cheng, X. Zhou, C. Yang, J. Xu and W. Zhou, *RSC Adv.*, 2023, **13**, 11938-11947.
114. B. Palas and G. Ersöz, *J. Mol. Liq.*, 2024, **394**, 123717.
115. Y. Wang, H. Xu and X. Zhang, *Adv. Mater.*, 2009, **21**, 2849-2864.
116. W. Dai, L. Jiang, J. Wang, Y. Pu, Y. Zhu, Y. Wang and B. Xiao, *Chem. Eng. J.*, 2020, **397**, 125476.
117. H. Zhu, L. Gou, C. Li, X. Fu, Y. Weng, L. Chen, B. Fang, L. Shuai and G. Liao, *Device*, 2024, **2**, 100283.
118. C. Li, X. Liu, P. Huo, Y. Yan, G. Liao, G. Ding and C. Liu, *Small*, 2021, **17**, 2102539.
119. Y.-J. Zhang, J.-Z. Cheng, Y.-Q. Xing, Z.-R. Tan, G. Liao and S.-Y. Liu,

View Article Online
DOI: 10.1039/D5MH01487E

Mater. Sci. Semicond. Proc., 2023, **161**, 107463.

120. A. Muzammil, R. Haider, W. Wei, Y. Wan, M. Ishaq, M. Zahid, W. Yaseen and X. Yuan, *Mater. Horiz.*, 2023, **10**, 2764-2799.
121. G. Liao, X. Tao and B. Fang, *Matter*, 2022, **5**, 377-379.
122. G. Liao, Y. Gong, L. Zhang, H. Gao, G.-J. Yang and B. Fang, *Energy Environ. Sci.*, 2019, **12**, 2080-2147.
123. P. Chen, L. Blaney, G. Cagnetta, J. Huang, B. Wang, Y. Wang, S. Deng and G. Yu, *Environ. Sci. Technol.*, 2019, **53**, 1564-1575.
124. T. Sun, J. Song, J. Jia, X. Li and X. Sun, *Nano Energy*, 2016, **26**, 83-89.
125. H. Ding, Z. Wang, K. Kong, S. Feng, L. Xu, H. Ye, W. Wu, X. Gong and J. Hua, *J. Mater. Chem. A*, 2021, **9**, 7675-7683.
126. J. Yang, J. Jing, W. Li and Y. Zhu, *Adv. Sci.*, 2022, **9**, 2201134.
127. H. Xu, Z. Wang, S. Feng, X. Liu, X. Gong and J. Hua, *Int. J. Hydrogen Energy*, 2023, **48**, 8071-8081.
128. W. Yu, N. Fang, Z. Liu, Y. Chu and B. Lai, *Small*, 2024, **20**, 2407104.
129. Z. Chen, D. Yan, X. Wang, G. Ding, Z. Wang, Y. Xiao, X. Liu, P. Wang, L. Chen, L. Shuai and G. Liao, *ACS Catal.*, 2025, **15**, 13568-13580.
130. J. Li, J. Fang, H. Liang, Z. Wei, J. Fang, L. Qiu, X. Lu, F. Yang and G. Zeng, *Chem. Eng. J.*, 2025, 164628.
131. S. Peng, R. Wang, Y. Yang, S. Wang, E. Liang, B. Han, J. Li, X. Yu and Q. Zhang, *Macromol. Rapid Commun.*, 2025, **46**, 2400967.
132. Y. Sheng, W. Li, L. Xu and Y. Zhu, *Adv. Mater.*, 2022, **34**, 2102354.
133. W. Li, Z. Wei, Y. Sheng, J. Xu, Y. Ren, J. Jing, J. Yang, J. Li and Y. Zhu, *ACS Energy Lett.*, 2023, **8**, 2652-2660.
134. G. Ding, C. Li, L. Chen and G. Liao, *Energy Environ. Sci.*, 2024, **17**, 5311-5335.
135. G. Liao, G. Ding, B. Yang and C. Li, *Precis. Chem.*, 2024, **2**, 49-56.
136. K. Liu, M. A. Nawaz and G. Liao, *Coordin. Chem. Rev.*, 2025, **535**, 216611.
137. G. Ding, C. Li, Y. Ni, L. Chen, L. Shuai and G. Liao, *EES Catal.*, 2023, **1**, 369-391.
138. Z. Chen, G. Ding, Z. Wang, Y. Xiao, X. Liu, L. Chen, C. Li, H. Huang and G. Liao, *Adv. Funct. Mater.*, 2025, **35**, 2423213.
139. F. Tian, X. Wu, J. Chen, X. Sun, X. Yan and G. Liao, *Dalton Trans.*, 2023, **52**, 11934-11940.
140. K. Liu, Y. Liao, P. Wang, X. Fang, J. Zhu, G. Liao and X. Xu, *Nanoscale*, 2024, **16**, 11096-11108.
141. Z. Zhao, F. Niu, P. Li, H. Wang, Z. Zhang, G. J. Meyer and K. Hu, *J. Am. Chem. Soc.*, 2022, **144**, 7043-7047.
142. W. Wu, H. Bi, Z. Zhang, L. Sun, R. Wei, L. Gao, X. Pan, J. Zhang and G. Xiao, *Colloids Surfaces A: Physicochem. Eng. Aspects*, 2023, **657**, 130486.
143. R. Yang, Q. Li, Z. Ma, S. Liu, D. Tian, D. Li and D. Jiang, *Chem. Eng. J.*, 2025, **506**, 160043.
144. R. Dalapati, M. Hunter, M. Sk, X. Yang and L. Zang, *ACS Appl. Mater. Interfaces*, 2024, **16**, 32344-32356.

145. S. Zheng, H. Du, L. Yang, M. Tan, N. Li, Y. Fu, D. Hao and Q. Wang, *J. Hazard. Mater.*, 2023, **447**, 130849.
146. Y. Li, Y.-H. Li, P. Wang, C. Zhao, C.-Y. Tang, S.-J. Gao and C.-C. Wang, *J. Environ. Chem. Eng.*, 2023, **11**, 109205.
147. F. M. A. Altalbawy, P. Sharma, F. H. Alsultany, A. Kumar, K. P. Vinay, I. S. Alalaq, M. Chahar, U. S. Altimari, A. m. Jabbar, M. M. Alam and L. H. Alzubaidi, *J. Mol. Struct.*, 2025, **1326**, 141088.
148. C. Zhu, C. Gong, D. Cao, L.-L. Ma, D. Liu, L. Zhang, Y. Li, Y. Peng and G. Yuan, *Angew. Chem. Int. Ed.*, 2025, **64**, e202504348.
149. M. Philippi, K. Kitzinger, J. S. Berg, B. Tschitschko, A. T. Kidane, S. Littmann, H. K. Marchant, N. Storelli, L. H. E. Winkel, C. J. Schubert, W. Mohr and M. M. M. Kuypers, *Nat. Commun.*, 2021, **12**, 4774.
150. S. Zhang, Y. Zhao, R. Shi, C. Zhou, G. I. N. Waterhouse, Z. Wang, Y. Weng and T. Zhang, *Angew. Chem. Int. Ed.*, 2021, **60**, 2554-2560.
151. Z. Lu, J. Zhang, Y. Wang, Y. Yu and L. Kong, *Mater. Horiz.*, 2025, **12**, 3286-3300.
152. M. Sharma, A. Kumar, D. Sajwan, K. Kumari, B. P. Mishra and V. Krishnan, *Adv. Sustainable Syst.*, 2025, **9**, 2400903.
153. J. S. Anderson, J. Rittle and J. C. Peters, *Nature*, 2013, **501**, 84-87.
154. G. Liao, C. Li, S.-Y. Liu, B. Fang and H. Yang, *Phys. Rep.*, 2022, **983**, 1-41.
155. G. Liao, C. Li, S.-Y. Liu, B. Fang and H. Yang, *Trends Chem.*, 2022, **4**, 111-127.
156. Q. Dong, X. Li, Y. Duan, X. He, X. Liang, F. Yu and C. Wang, *Appl. Catal. B: Environ. Energy*, 2025, **366**, 125042.
157. D. Zhu, L. Zhang, R. E. Ruther and R. J. Hamers, *Nat. Mater.*, 2013, **12**, 836-841.
158. Q. Li, D. Shen, Z. Xiao, X. Liu, X. Xu, M. Wu, W. Wang, L. Liu, Q. Li and X. Li, *Small*, 2025, **21**, 2411665.
159. S. Yang, X. Deng, P. Chen, G. Li, Q. Wang, Q. Wang and S.-F. Yin, *Chem. Eng. J.*, 2022, **441**, 136084.
160. Q. Wang, J. Cao, P. Chen, S. Yang, C. Fu, F. Liu and S.-F. Yin, *Appl. Catal. A: Gen.*, 2023, **649**, 118978.
161. D. Cui, X. Yang, Y. Liu, M. Li, C. Wang and F. Li, *Sep. Purif. Technol.*, 2025, **356**, 130035.
162. Y. Qiao, C. Sun, J. Jian, T. Zhou, X. Xue, J. Shi, G. Che and G. Liao, *J. Mol. Liquids*, 2023, **385**, 122383.
163. G. Ding, Z. Wang, J. Zhang, P. Wang, L. Chen and G. Liao, *EcoEnergy*, 2024, **2**, 22-44.
164. C. Du, J. Xu, G. Ding, D. He, H. Zhang, W. Qiu, C. Li and G. Liao, *Nanomaterials*, 2023, **13**, 3066.
165. W. Zhou, G. Liu, B. Yang, Q. Ji, W. Xiang, H. He, Z. Xu, C. Qi, S. Li, S. Yang and C. Xu, *Sci. Total Environ.*, 2021, **780**, 146483.
166. Q. Wu, J. Wang, Z. Wang, Y. Xu, Z. Xing, X. Zhang, Y. Guan, G. Liao and X. Li, *J. Mater. Chem. A*, 2020, **8**, 13685-13693.

167. S. Liu, F. Deng, Y. Guo, C. Ouyang, S. Yi, C. Li, G. Liao and Q. Li, *ACS Appl. Nano Mater.*, 2024, **7**, 889-903.
168. G. Liao, Y. Gong, L. Zhong, J. Fang, L. Zhang, Z. Xu, H. Gao and B. Fang, *Nano Res.*, 2019, **12**, 2407-2436.
169. G. Liao, J. Fang, Q. Li, S. Li, Z. Xu and B. Fang, *Nanoscale*, 2019, **11**, 7062-7096.
170. Z. Lu, B. Li, B. Wei, G. Zhou, Y. Xu, J. Zhang, H. Chen, S. Hua, C. Wu and X. Liu, *Sep. Purif. Technol.*, 2023, **314**, 123609.
171. Z. Mao, P. Luo, J. Ling, X. Zhu, K. Sun, Y. Cao, D. Zhu and W. Liu, *J. Alloy. Compd.*, 2025, **1011**, 178195.
172. K. Zha, L. Li, J. Zhang, S. Tang, X. Li, J. Hai, D. Fan, M. Li, Y. Liu and Z. Lu, *J. Photochem. Photobiol. A: Chem.*, 2024, **451**, 115517.
173. X. Zhang, L. Shi and Y. Zhang, *J. Taiwan Inst. Chem. Eng.*, 2022, **132**, 104111.
174. X. Zhang, L. Shi, L. Yao and L. Cui, *Mater. Res. Bull.*, 2022, **146**, 111589.
175. T. Xu, S. Zhang, W. Zhang and L. Shi, *Opt. Mater.*, 2024, **147**, 114656.
176. H. Miao, J. Yang, Y. Sheng, W. Li and Y. Zhu, *Solar RRL*, 2021, **5**, 2000453.
177. Z. Liang, R. Shen, P. Zhang, Y. Li, N. Li and X. Li, *Chinese J. Catal.*, 2022, **43**, 2581-2591.
178. J. Yang, H. Miao, J. Jing, Y. Zhu and W. Choi, *Appl. Catal. B: Environ.*, 2021, **281**, 119547.
179. C. Ye, J.-X. Li, H.-L. Wu, X.-B. Li, B. Chen, C.-H. Tung and L.-Z. Wu, *ACS Appl. Mater. Interfaces*, 2018, **10**, 3515-3521.
180. L. Liu, J. Liu, S. Zong, Z. Huang, X. Feng, J. Zheng and Y. Fang, *Int. J. Hydrogen Energy*, 2022, **47**, 39486-39498.
181. S. Chen, C. Wang, B. R. Bunes, Y. Li, C. Wang and L. Zang, *Appl. Catal. A: Gen.*, 2015, **498**, 63-68.
182. X. Li, X. Lv, Q. Zhang, B. Huang, P. Wang, X. Qin, X. Zhang and Y. Dai, *J. Colloid Interface Sci.*, 2018, **525**, 136-142.
183. J. Chen, W. Lin, J. Lin and Y. Wang, *J. Mater. Chem. A*, 2025, **13**, 1095-1101.
184. X. Ji, X. Liu, Y. Guo and J. Zhang, *Chem. Eng. J.*, 2021, **425**, 131260.
185. H. Zhuang, F. Wang, K. Shi and K. Yang, *Catalysts*, 2023, **13**, 688.
186. Y. Jia, L. Duan, H. Li, C. Zhang, Q. Gao, H. Zhang, S. Li and M. Li, *Sep. Purif. Technol.*, 2025, **358**, 130292.
187. Z. Zhang, J. Liu, P.-Y. Gu, R. Ji, L. Jin, S. Zhou, J. He, D. Chen, Q. Xu and J. Lu, *Sep. Purif. Technol.*, 2022, **287**, 120539.